Stability and Convergence of a Regularized Immersed Boundary Method under Dynamic Cartesian Refinement. Part III: Fluid-Driven Rigid-Body Motion

Sida He
Huawei Technologies Co., Ltd.
hesida1@huawei.com
ORCID: 0000-0003-0849-6592

27 October 2026
Research preprint, version 0.1.1

hexagon:2610.00593v1

Disclosure: Primarily AI-generated text. The author reports no understanding of the proofs; see the disclosure at the end of this manuscript.

Abstract

We study a conforming regularized immersed boundary discretization of the two-dimensional Eulerian Stokes–Newton system for one freely moving rigid body. Regularized interior moments complete the surface constraints used for prescribed motion. Positive excess mass and inertia define a fixed fluid–body kinetic inner product. A skew inertial correction is derived from the fictitious rigid interior; it has zero power but is necessary for the physical translational momentum equation. The method advances the body configuration with the preceding computed rigid velocity and then solves a linear joint fluid–body step on a dynamically enriched Cartesian space. Exact orthogonal transfer gives an energy identity independent of the number of mesh changes. Interior and surface moment defects control the discrepancy between the discrete background energy and physical kinetic energy. A volume-preserving geometry comparison and a moving coarse recovery family yield conditional joint convergence of the fluid velocity, rigid velocity, and body configuration on an interval with positive wall clearance. The error bound distinguishes the energy norm after geometry alignment from the generally weaker estimate at the same Eulerian points. The analysis assumes exact integration and explicit strong-solution regularity; it does not cover arbitrary density ratios or collisions. Manufactured coupled computations, independent residual checks, and a Lean algebraic companion document the numerical and formal verification scope.

Keywords: immersed boundary method; rigid-body interaction; dynamic Cartesian refinement; fictitious inertia; geometric error; energy stability; convergence.

1 Introduction and scope

Regularized immersed boundary methods couple Eulerian fluid variables to a separately represented structure through regularized interpolation and its adjoint force spreading [1]. Parts I and II of this series [2, 3] analyzed one conforming Cartesian realization under arbitrary

changes of local enrichments, first for fixed interfaces and then for prescribed rigid motion. This paper makes the rigid motion an unknown. Translation and rotation are determined by Newton's equations, and the numerical body configuration therefore differs from the exact one. A convergence argument must control that difference jointly with the fluid error.

The passage from prescribed to computed motion requires more than inserting a numerical trajectory into the estimates of Part II. There the fictitious interior forcing was chosen to reproduce a known rigid acceleration. Here that acceleration is unknown. Surface constraints alone do not identify the interior fluid momentum with the displaced rigid momentum. Fictitious-domain formulations enforce interior rigidity and account for displaced-fluid inertia [4, Section 4]; the interior-inertia issue is also explicit in regularized rigid-body IB formulations [5, Section II]. Accordingly, we add regularized *volume* moments to the regularized surface moments of Part II. The discrete interior is only approximately rigid. Its defect is estimated rather than silently identified with zero.

There is substantial prior analysis of fluid-driven rigid motion. San Martín et al. proved convergence of a fixed-mesh Lagrange–Galerkin method [6]. Legendre and Takahashi derived joint fluid, rigid-velocity, and configuration error estimates in an ALE formulation [7, Theorem 3.5 and Section 4]. Discontinuous-density global formulations [8] and free-body penalization convergence [9] provide other established approaches. In a fully Eulerian unfitted setting, von Wahl and Richter analyzed a coupled vector-valued parabolic equation and translational-motion ODE, including dynamic domain error [10]. Their model omits the fluid divergence constraint and body rotation, but its comparison of numerical and exact geometry is a direct methodological precedent. Thus neither coupled rigid-body convergence nor geometry comparison is claimed to originate here.

Our energy argument builds on the usual cancellation of interface power in multiplier formulations [11, 12]. The background kinetic inner product uses positive *excess* mass and inertia. These assumptions restrict the present analysis to sufficiently heavy bodies; they do not describe a physical instability of lighter bodies. An additional skew term is needed because the fluid equation uses the Eulerian Stokes derivative, not the Navier–Stokes material acceleration. We derive that term explicitly from the rigid interior. Its power vanishes, but omitting it would change the translational momentum equation.

The numerical spaces and transfer principles retain the architecture of Parts I–II. Dynamic-space Stokes projection estimates [13], stable adaptive transfers [14], and moving-boundary remeshing analysis [15] supply the relevant context. We use exact orthogonal projection in a fixed fluid–body mass inner product. Every admissible local enrichment retains the entire coarse Cartesian streamfunction space. A constructed coarse comparison then removes any factor counting refinement and coarsening events. The method does not include an error-based marking rule, and the coarse grid itself is refined in a convergence sequence. Optimal adaptive fictitious-domain and regularized-forcing results [16, 17] address different questions.

Regularized IB convergence results of Mori and Liu–Mori [18–20], and prescribed-velocity Stokes estimates of Li et al. [21], motivate careful separation of bulk accuracy from boundary enforcement. Our constraints use exact continuum convolution and cell moments, rather than a particular sampled delta stencil. Regularization estimates [22] and Sobolev trace and approximation results [23] are used explicitly in the defect bounds. The background velocity spaces are generated by conforming bicubic Hermite streamfunctions [24]; the theorem is not a convergence theorem for a conventional staggered-grid AMR solver. Adaptive IB computations [25] and the dynamically adaptive DLM–IB framework of Zeng et al. [26] predate this analysis and use different implementations.

For moving fluid equations, evolving-space formulations [27, 28], Eulerian unfitted analyses [29–31], and ALE error estimates [32] provide further context. We use an auxiliary volume-

preserving map to compare the exact and computed body configurations. This map is part of the proof, not a transport step in the algorithm. In particular, the square-root continuity of a trace with respect to interface displacement is not by itself a closed estimate for an unknown trajectory. Geometry alignment must first produce residuals linear in the configuration error.

Computational studies also illustrate why boundary and force consistency deserve separate attention. He et al. developed an immersed pressure treatment to mitigate penetration through thin flexible structures in multiphase flow [33]. Zheng et al. studied prescribed flapping near a free surface [34]. IB calculations of backward-facing-step flow [35], airfoil transition [36], and flexible canopies [37] give additional application context. These turbulent, multiphase, or deformable configurations are outside the present model; their numerical observations are not premises of our proofs.

The result concerns one planar rigid body on an interval with positive wall clearance, positive excess mass and inertia, and a sufficiently regular exact Stokes–Newton solution. It is a numerical analysis conditional on that solution, not a new general existence theorem. The distinction between energy error after geometry alignment and energy error at the same Eulerian points is retained throughout: moving a gradient jump can weaken the latter estimate. Exact integration is assumed in the theorem. Numerical quadrature, finite-precision constraints, and selected algebraic identities are checked independently in the computational and Lean companions.

2 A physical rigid-body model and its whole-box extension

2.1 Exterior Stokes flow coupled to Newton's equations

Let $\Omega = (0,1)^2$ and let $B_* \Subset \mathbb{R}^2$ be a fixed simply connected body with connected C^6 boundary and centroid zero: $\int_{B_*} x\,dx = 0$. The body mass center is assumed to coincide with this geometric centroid. Write

$$J = \begin{pmatrix} 0 & -1 \\ 1 & 0 \end{pmatrix}, \qquad Q(\theta) = \begin{pmatrix} \cos\theta & -\sin\theta \\ \sin\theta & \cos\theta \end{pmatrix}.$$

For a pose $q = (c, \theta)$, define $B(q) = c + Q(\theta)B_*$, $F(q) = \Omega \setminus \overline{B(q)}$, and $\Gamma(q) = \partial B(q)$. The normal n_q points out of the body into the fluid. The analysis concerns a smooth solution branch on $[0,T]$ for which the body has a positive clearance from the outer wall. Quantitative regularity assumptions used for convergence are stated below; no convergence of numerical geometries is assumed.

Let the fluid density and viscosity be $\rho_f > 0$ and $\mu > 0$. The physical body mass and scalar moment of inertia about c are $m_s > 0$ and $I_s > 0$. With $\xi = (V, \omega)$, set

$$\mathcal{R}_q\xi(x) = V + \omega J(x - c), \qquad b(t,x) = \mathcal{R}_{q(t)}\xi(t)(x).$$

The pose satisfies

$$\dot{c} = V, \qquad \dot{\theta} = \omega. \tag{1}$$

The exterior fluid equations, with an *Eulerian* time derivative, are

$$\begin{aligned} \rho_f \partial_t u - \operatorname{div}\sigma &= f && \text{in } F(q(t)), \\ \operatorname{div} u &= 0, \quad \sigma = 2\mu D(u) - pI, && D(u) = \tfrac{1}{2}(\nabla u + \nabla u^{\mathsf{T}}), \\ u &= 0 && \text{on } \partial\Omega, \\ u &= b && \text{on } \Gamma(q(t)). \end{aligned} \tag{2}$$

Here $f(t,x)$ is a given ambient extension of the exterior force density, whose restriction to $F(q(t))$ is used in the equation. The external force and torque on the body are denoted by $F_e(t)$ and $T_e(t)$. Newton's equations are

$$\begin{aligned} m_s\dot{V} &= F_e + \int_{\Gamma(q)} \sigma n_q \, ds, \\ I_s\dot{\omega} &= T_e + \int_{\Gamma(q)} J(x-c)\cdot \sigma n_q \, ds. \end{aligned} \tag{3}$$

The fluid traction in these equations is the exterior stress acting on the body. We do not replace it by an uncorrected force spread over a fictitious interior.

Define the mass and inertia of the fluid displaced by the body, and their excess-body counterparts, by

$$\begin{aligned} m_f &= \rho_f |B_*|, & I_f &= \rho_f \int_{B_*} |x|^2 \, dx, \\ m_e &= m_s - m_f > 0, & I_e &= I_s - I_f > 0. \end{aligned} \tag{4}$$

The strict inequalities are assumptions of the method analyzed here. For a homogeneous body they follow from a solid density larger than the fluid density. They make the discrete background-domain mass form positive even before interior rigidity is accurately enforced. The result does not cover zero or negative excess inertia.

2.2 The fixed positive product space

Let

$$U = \{v \in H_0^1(\Omega)^2 : \operatorname{div} v = 0\}, \qquad \|v\|_U = \|\nabla v\|_{L^2(\Omega)}, \qquad \mathbb{V} = U \times \mathbb{R}^2 \times \mathbb{R}.$$

The ambient kinetic-energy space is $\mathbb{H} = L^2(\Omega)^2 \times \mathbb{R}^2 \times \mathbb{R}$. For $X = (u, V, \omega)$ and $Y = (v, W, \eta)$, define

$$(X,Y)_M = \rho_f (u,v) + m_e V \cdot W + I_e \omega\eta, \qquad \|X\|_M^2 = (X,X)_M. \tag{5}$$

The inner product is independent of the pose and of every mesh and moment partition. The viscous and gyroscopic forms are

$$a(u,v) = 2\mu (D(u), D(v)), \qquad \mathcal{G}(\varpi; X, Y) = m_f \varpi(JV)\cdot W. \tag{6}$$

For $u, v \in U$, integration by parts gives $a(u,v) = \mu(\nabla u, \nabla v)$ on the whole box. Also $\mathcal{G}(\varpi; X, Y) = -\mathcal{G}(\varpi; Y, X)$, and $\mathcal{G}(\varpi; X, X) = 0$.

Extend the physical fluid velocity into the body by $u = b$ and define the continuous joint constraint space

$$\mathbb{K}(q) = \{(v, W, \eta) \in \mathbb{V} : v = \mathcal{R}_q(W, \eta) \text{ a.e. in } B(q)\}. \tag{7}$$

The extension belongs to U because the exterior and interior traces match. Its distributional time derivative contains no surface delta: the coefficient of such a term would be the velocity jump, which is zero. The exact joint state lies in $\mathbb{K}(q(t))$. For any joint test Y, let

$$\mathcal{L}(t, q; Y) = \int_{F(q)} f(t,x)\cdot v(x)\, dx + F_e(t)\cdot W + T_e(t)\eta. \tag{8}$$

Proposition 2.1 (The Eulerian fictitious-inertia correction)**.** *For a sufficiently regular collision-free solution of (2)–(3), the rigid extension satisfies*

$$(\partial_t X, Y)_M + a(u,v) + \mathcal{G}(\omega; X, Y) = \mathcal{L}(t, q; Y), \qquad Y \in \mathbb{K}(q(t)). \tag{9}$$

Conversely, the sufficiently regular constrained formulation (1), (9) gives the exterior Stokes and physical Newton equations, with the exterior pressure and traction understood in their usual weak sense.

Proof. Since $c' = V$, the Eulerian interior derivative is

$$\partial_t b = \dot{V} + \dot{\omega} J(x - c) - \omega J V. \tag{10}$$

For a rigid interior test $v = W + \eta J(x - c)$, the zero-centroid condition and rigid invariance of area and polar moment imply

$$\rho_f \int_{B(q)} \partial_t b \cdot v \, dx = m_f(\dot{V} - \omega J V) \cdot W + I_f \dot{\omega} \eta. \tag{11}$$

Thus the whole-box fluid inertia, the excess body inertia, and $\mathcal{G}(\omega; X, Y)$ sum to the exterior fluid inertia plus $m_s \dot{V} \cdot W + I_s \dot{\omega} \eta$. The strain of the rigid extension is zero in the body, so the whole-box viscous form equals the exterior viscous form for these states and tests. Integration of the exterior fluid equation by parts produces the traction work $\int_\Gamma \sigma n_q \cdot \mathcal{R}_q(W, \eta)$ on the left. Substituting (3) proves (9).

Conversely, tests with zero rigid component and fluid support in the exterior give the Stokes equation. Any rigid test velocity admits a solenoidal, outer-zero extension: multiply its affine/quadratic streamfunction by a cutoff equal to one near the body and take its curl. Subtracting the exterior fluid weak identity for these tests from (9), and using (11), gives both equations in (3). □

The extra term $m_f \omega J V$ is necessary for the Eulerian Stokes model. Excess-inertia formulas derived with a material acceleration, as in the classical distributed-multiplier formulation [4, Section 4], cannot be transferred unchanged after deleting advection. For the present planar rigid motion, this additional term is gyroscopic and contributes no kinetic-energy work.

2.3 Volume and surface reactions

For consistency estimates we need an identity on the full test space, not only on exactly rigid tests. Under the same regularity, choose the interior pressure to be zero and set

$$\lambda_B = -\rho_f \partial_t b \quad \text{in } B(q), \qquad \lambda_\Gamma = \sigma n_q \quad \text{on } \Gamma(q). \tag{12}$$

Then, for every $Y = (v, W, \eta) \in \mathbb{V}$, with $\zeta = (W, \eta)$,

$$\begin{aligned}(\partial_t X, Y)_M + a(u, v) + \mathcal{G}(\omega; X, Y) + \int_{B(q)} \lambda_B \cdot (v - \mathcal{R}_q \zeta) \, dx \\ + \int_{\Gamma(q)} \lambda_\Gamma \cdot (\gamma_q v - \mathcal{R}_q \zeta) \, ds = \mathcal{L}(t, q; Y).\end{aligned} \tag{13}$$

Indeed, the volume reaction cancels the fictitious interior fluid inertia in the fluid equation. In the rigid equation its opposite work restores the displaced-fluid inertia in (11); the gyroscopic term restores the remaining $m_f \omega J V$. The surface reaction supplies the physical exterior traction. This proves the identity by direct substitution, without an inf–sup or multiplier-convergence theorem. The displayed pair is one convenient continuous representative; neither uniqueness of all reaction representations nor convergence of discrete multipliers is needed below.

Surface velocity constraints alone do not ensure that an unsteady fictitious interior has the rigid angular momentum used in (11); this issue is also discussed by Kallemov et al. [5]. The discrete method therefore uses both volume and surface moments. At a finite resolution its interior rigidity is approximate, and its positive energy must be interpreted as a surrogate, as quantified in Proposition 3.3.

2.4 Physical energy of the continuous model

For an exactly rigid extended state, the mass energy is precisely the physical kinetic energy:

$$\tfrac{1}{2}\|X\|_M^2 = \frac{\rho_f}{2}\int_{F(q)} |u|^2\,dx + \frac{m_s}{2}|V|^2 + \frac{I_s}{2}\omega^2. \tag{14}$$

Testing (9) by X gives

$$\frac{d}{dt}\frac{1}{2}\|X\|_M^2 + a(u,u) = \mathcal{L}(t,q;X). \tag{15}$$

The moving exterior does not leave an unaccounted kinetic-energy flux in this identity. On the interface $u = b$ and

$$\int_{\Gamma(q)} |b|^2 b\cdot n_q\,ds = \int_{B(q)} \operatorname{div}(|b|^2 b)\,dx = 0,$$

because $\operatorname{div} b = 0$ and $b\cdot(\nabla b)b = b\cdot(\omega J)b = 0$ pointwise. The Reynolds-transport boundary term therefore vanishes after integration. Finally $D(u) = 0$ in the rigid interior, so $a(u,u) = 2\mu\int_{F(q)}|D(u)|^2$ is the physical fluid dissipation.

3 Regularized volume and surface constraints

The surface-only constraints of Parts I–II are completed by interior moments. This is a change of the discrete method, not an inference that surface no-slip makes the fictitious interior rigid. Interior constraints are standard in fictitious-domain rigid-body formulations [4, 5]; the particular regularized moments and their defects are specified here.

Let $\xi = (V,\omega)$ and write $\mathcal{R}_q\xi(x) = V + \omega J(x-c)$. For $v \in U$, let Ev be its zero extension and set $\mathcal{J}_\varepsilon v = \rho_\varepsilon * Ev$, where ρ is the nonnegative, even, smooth unit-mass kernel supported in the unit ball used in Part II. All kernel supports considered below stay inside Ω. Let $\mathcal{C}$ partition $B(q)$ into volume cells, with maximum diameter κ, and let $\mathcal{P}$ partition $\Gamma(q)$ into arclength panels, with maximum length ℓ. We require the local Poincare inequality

$$\|z - z_C\|_{L^2(C)} \le C_{\mathrm{vol}}\kappa\|\nabla z\|_{L^2(C)}, \qquad z_C = |C|^{-1}\int_C z,$$

with one constant for all volume cells and runs. Convex cells have such a diameter bound even when they are thin, by the Payne–Weinberger inequality [38]. In particular, a convex reference body intersected with Cartesian squares, followed by the rigid map, provides admissible partitions. For a nonconvex smooth body one may use transported reference partitions satisfying this inequality. Denote volume and surface cell-average projectors by $\Pi_{\mathcal{C}}$ and $\Pi_{\mathcal{P}}$.

In the retained-coarse Cartesian velocity space $X_{h,\mathcal{A}}$ of Part II, define the linear joint constraint space

$$\begin{aligned}\mathbb{K}_h(q) = \{(v_h,\zeta)\in X_{h,\mathcal{A}}\times\mathbb{R}^3 :\ & \Pi_{\mathcal{C}}(\mathcal{J}_\varepsilon v_h - \mathcal{R}_q\zeta) = 0,\\ & \Pi_{\mathcal{P}}\gamma_q(\mathcal{J}_\varepsilon v_h - \mathcal{R}_q\zeta) = 0\}.\end{aligned} \tag{16}$$

The parameters $\mathcal{A},\varepsilon,\mathcal{C},\mathcal{P}$ are suppressed in the notation and may change at every step. These are exact integral constraints in the theorem; their quadrature realization is assessed separately in the numerical section. They neither assume nor imply linear independence of multiplier rows. Throughout, $\bar\varepsilon$, $\bar\kappa$, and $\bar\ell$ denote maxima over all configurations of a run, including the initialization at $n = 0$.

The coarse lift $L_{h,q}\zeta$ of Lemma 4.1 equals $\mathcal{R}_q\zeta$ throughout the body and all relevant kernel supports, and satisfies

$$\|L_{h,q}\zeta\|_U \le C|\zeta|.$$

Consequently $(L_{h,q}\zeta, \zeta) \in \mathbb{K}_h(q)$ for every ζ, irrespective of the local enrichment or moment partitions. For $Y_h = (v_h, \zeta) \in \mathbb{K}_h(q)$, put $w_h = v_h - L_{h,q}\zeta$ and $\|Y_h\|_{\mathbb{V}} = \|v_h\|_U + |\zeta|$.

Lemma 3.1 (Interior rigidity and physical surface defects)**.** *Uniformly over the admissible configurations and partitions,*

$$\|v_h - \mathcal{R}_q\zeta\|_{L^2(B(q))} \le C(\varepsilon + \kappa)\|Y_h\|_{\mathbb{V}}, \tag{17}$$

$$\|\gamma_q v_h - \mathcal{R}_q\zeta\|_{L^2(\Gamma(q))} \le C(\sqrt{\varepsilon} + \sqrt{\ell})\|Y_h\|_{\mathbb{V}}. \tag{18}$$

Proof. Polynomial reproduction by the lift and the zero first moment of the kernel give $\Pi_{\mathcal{C}}\mathcal{J}_\varepsilon w_h = 0$ and $\Pi_{\mathcal{P}}\gamma_q\mathcal{J}_\varepsilon w_h = 0$. The first-order mollification estimate and Young's inequality [22, Lemmas 3–4] imply

$$\|w_h - \mathcal{J}_\varepsilon w_h\|_{L^2(\Omega)} \le C\varepsilon\|w_h\|_U, \qquad \|\nabla\mathcal{J}_\varepsilon w_h\|_{L^2(\mathbb{R}^2)} \le \|w_h\|_U.$$

Apply the volume-cell Poincare inequality to $\mathcal{J}_\varepsilon w_h$ and sum its squared bounds. The triangle inequality proves $\|w_h\|_{L^2(B(q))} \le C(\varepsilon + \kappa)\|w_h\|_U$. On $B(q)$, $w_h = v_h - \mathcal{R}_q\zeta$.

The multiplicative trace estimate on a uniform tubular neighborhood gives $\|\gamma_q(w_h - \mathcal{J}_\varepsilon w_h)\|_{L^2(\Gamma(q))} \le C\sqrt{\varepsilon}\|w_h\|_U$. The fractional Poincare inequality on the panels, together with the uniform $H^{1/2}$ trace bound for $\mathcal{J}_\varepsilon w_h$, gives $\|\gamma_q\mathcal{J}_\varepsilon w_h\|_{L^2(\Gamma(q))} \le C\sqrt{\ell}\|w_h\|_U$. These are precisely the fixed-configuration ingredients of the trace proof in Part II [3]; see also Ern and Guermond [23, Theorem 3.10, Lemmas 3.26 and 12.15]. Finally $\|w_h\|_U \le C\|Y_h\|_{\mathbb{V}}$ proves both claims. □

Lemma 3.2 (Uniform control of rigid test velocities)**.** *There is $\kappa_0 > 0$, independent of the fluid mesh and regularization width, such that, for $\kappa \le \kappa_0$ and $(v_h, \zeta) \in \mathbb{K}_h(q)$,*

$$|\zeta| \le C\|v_h\|_{L^2(\Omega)} \le C\|v_h\|_U, \qquad \|(v_h, \zeta)\|_{\mathbb{V}} \le C\|v_h\|_U.$$

Proof. Since the reference centroid is zero,

$$\|\mathcal{R}_q(W, \eta)\|^2_{L^2(B(q))} = |B_*||W|^2 + \left(\int_{B_*} |x|^2 dx\right)|\eta|^2 \ge c_B^2|(W, \eta)|^2$$

for a fixed $c_B > 0$. The volume constraint, contractivity of the cell average projector, and convolution boundedness imply

$$\|\Pi_{\mathcal{C}}\mathcal{R}_q\zeta\|_{L^2(B(q))} = \|\Pi_{\mathcal{C}}\mathcal{J}_\varepsilon v_h\|_{L^2(B(q))} \le \|v_h\|_{L^2(\Omega)}.$$

The cell Poincare inequality applied to the affine rigid field gives $\|(I - \Pi_{\mathcal{C}})\mathcal{R}_q\zeta\|_{L^2(B(q))} \le C\kappa|\eta|$. Thus $c_B|\zeta| \le \|v_h\|_0 + C\kappa|\zeta|$. Choose $C\kappa_0 \le c_B/2$ and absorb the last term. The fixed-box Poincare inequality completes the proof. □

Proposition 3.3 (What the discrete energy represents)**.** *For a joint state $X_h = (u_h, V_h, \omega_h) \in \mathbb{K}_h(q)$, let $E_M(X_h) = \frac{1}{2}\|X_h\|^2_M$ be the positive background-domain energy from Section 2, and define*

$$E_{\mathrm{phys}}(X_h; q) = \frac{\rho_f}{2}\|u_h\|^2_{L^2(F(q))} + \frac{m_s}{2}|V_h|^2 + \frac{I_s}{2}|\omega_h|^2.$$

Then

$$E_M(X_h) - E_{\mathrm{phys}}(X_h; q) = \frac{\rho_f}{2}\int_{B(q)} (u_h - \mathcal{R}_q\xi_h)\cdot(u_h + \mathcal{R}_q\xi_h)\, dx. \tag{19}$$

In particular, bounds on $\max_n \|X_h^n\|_M$ and $\sum_n \tau_n\|X_h^n\|^2_{\mathbb{V}}$ imply

$$\sum_n \tau_n|E_M(X_h^n) - E_{\mathrm{phys}}(X_h^n; q_n)| \le C(\bar{\varepsilon} + \bar{\kappa}).$$

This statement alone is time-integrated; it does not assert uniform nodal convergence of the two energies.

Proof. The reference centroid is zero and rigid maps preserve area and polar moment. Thus $\rho_f \int_{B(q)} |\mathcal{R}_q \xi_h|^2 = m_f |V_h|^2 + I_f |\omega_h|^2$. Subtract the two definitions, use the excess masses $m_e = m_s - m_f$, $I_e = I_s - I_f$, and factor the difference of squares. Cauchy–Schwarz, (17), and the positive mass norm give the asserted time-integrated estimate. □

4 Joint recovery and alignment of two rigid configurations

Fix a compact family of collision-free configurations containing a neighborhood of the exact trajectory. All bodies in this family have a common positive clearance from the outer wall. Constants in this section are uniform on this family. Angles are represented by real continuous lifts, rather than reduced modulo 2π.

4.1 Retained Cartesian spaces and a joint lift

For $h = 1/M$, let $S_h \subset H_0^2(\Omega)$ be the clamped bicubic Hermite space on the uniform Cartesian grid. Its vertex data are $\psi, \psi_x, \psi_y, \psi_{xy}$. On an enriched coarse cell K, add the four center degrees of freedom of its subdivision into four squares, keeping the value and gradient zero on ∂K. Writing this local space as $B_h(K)$, set

$$X_{h,\mathcal{A}} = \operatorname{curl}\left(S_h + \sum_{K \in \mathcal{A}} B_h(K) \right), \qquad \operatorname{curl} \psi = (\psi_y, -\psi_x).$$

Every configuration contains $\operatorname{curl} S_h$ and is a conforming subspace of U. This is the concrete retained-coarse construction of Parts I–II, based on Cartesian Bogner–Fox–Schmit interpolation [3, 24]. Its coarse interpolant satisfies

$$\|I_h \psi - \psi\|_{H^j} \le C h^{4-j} \|\psi\|_{H^4}, \qquad j = 1, 2. \tag{20}$$

Choose a fixed $\chi \in C_c^5(\Omega)$ equal to one on a neighborhood of every body in the admissible configuration family. The plateau includes a fixed-width neighborhood of their union. With $x_* = (1/2, 1/2)$, $r = x - x_*$, and $\zeta = (W, \eta)$, put

$$\begin{aligned} \beta_q(\zeta) &= W - \eta J(c - x_*), \\ p_{q,\zeta}(x) &= \beta_{q,1}(\zeta) r_2 - \beta_{q,2}(\zeta) r_1 - \tfrac{1}{2}\eta |r|^2, \\ L_q \zeta &= \operatorname{curl}(\chi p_{q,\zeta}), \qquad L_{h,q} \zeta = \operatorname{curl} I_h(\chi p_{q,\zeta}). \end{aligned} \tag{21}$$

This fixes the additive normalization before multiplication by the cutoff. Direct differentiation gives $\operatorname{curl} p_{q,\zeta} = \mathcal{R}_q \zeta$.

Lemma 4.1 (A common joint rigid lift)**.** *For sufficiently small $h + \bar{\varepsilon}$, the coarse lift $L_{h,q}\zeta$ equals $\mathcal{R}_q \zeta$ on every admissible body and throughout every regularization support centered in that body or on its boundary. Consequently $(L_{h,q}\zeta, \zeta) \in \mathbb{K}_h(q)$, independently of the enrichments and both moment partitions. Uniformly in q,*

$$\|L_{h,q}\zeta\|_U \le C|\zeta|, \qquad \|(L_{h,q} - L_q)\zeta\|_U \le C h^2 |\zeta|, \quad \|(L_{h,q} - L_q)\zeta\|_0 \le C h^3 |\zeta|.$$

For a Lipschitz path $q(t)$ and $\zeta \in H^1(0, T; \mathbb{R}^3)$,

$$\|\partial_t [(L_{h,q(t)} - L_{q(t)})\zeta(t)]\|_{L_t^2 L_x^2} \le C h^3 (1 + \|q'\|_{L^\infty}) \|\zeta\|_{H_t^1}. \tag{22}$$

Proof. Every cell meeting a kernel support lies within $\bar{\varepsilon} + \sqrt{2}h$ of the admissible body union. On such cells $\chi p_{q,\zeta} = p_{q,\zeta}$, a quadratic reproduced exactly by Hermite interpolation. Unit mass and zero first moment of the kernel preserve its affine curl. The same argument covers interior cells. The estimates follow from (20); the coefficients of $p_{q(t),\zeta(t)}$ have H^1 time derivatives controlled by the right-hand side of (22). Only the fixed interpolant I_h is commuted with differentiation. □

4.2 Volume-preserving configuration alignment

The comparison follows the cutoff solenoidal-flow construction of Legendre and Takahashi [7, Section 4.1], together with the transformed rigid velocities in their Section 4.2. We give its realization and the continuous-time bounds needed for the present Cartesian recovery. For two sufficiently close configurations $q = (c, \theta)$ and $\widehat{q} = (\widehat{c}, \widehat{\theta})$, set $d_q = |\widehat{c} - c| + |\widehat{\theta} - \theta|$ and $O = Q(\widehat{\theta} - \theta)$. A comparison of velocities on the two different bodies must account for their geometry. Merely shifting a trace estimate would introduce $\sqrt{d_q}$ into the error equation and would not yield the Gronwall estimate used below.

Lemma 4.2 (Constructive solenoidal alignment)**.** *There is a smooth volume-preserving diffeomorphism $\Psi = \Psi(q, \widehat{q}) : \Omega \to \Omega$, equal to the identity near the outer wall and satisfying*

$$\Psi(x) = \widehat{c} + O(x - c) \quad \text{on a fixed-width neighborhood of } \overline{B(q)}. \tag{23}$$

For every fixed finite k, uniformly for small d_q,

$$\|\Psi - \mathrm{id}\|_{W^{k,\infty}} + \|\Psi^{-1} - \mathrm{id}\|_{W^{k,\infty}} \le C_k d_q. \tag{24}$$

For Lipschitz paths $q(t), \widehat{q}(t)$ with bounded speeds,

$$\|\partial_t \Psi\|_{W^{k,\infty}} \le C_k(d_q + |\widehat{q}' - q'|) \quad \text{a.e.} \tag{25}$$

The Piola map

$$(\mathcal{T}_\Psi v)(\Psi(x)) = D\Psi(x) v(x) \tag{26}$$

preserves U and maps the exact joint space at q to that at $\widehat{q}$, with rigid velocity transformed by $(V, \omega) \mapsto (OV, \omega)$.

Proof. Let $\Delta c = \widehat{c} - c$, $\Delta\theta = \widehat{\theta} - \theta$, $c_s = c + s\Delta c$, and $\theta_s = \theta + s\Delta\theta$, for $0 \le s \le 1$. Extend the rigid s-velocity $\Delta c + \Delta\theta J(x - c_s)$ by the compactly supported streamfunction formula (21), but use a separate auxiliary cutoff $\chi_A \in C_c^\infty(\Omega)$ with the same plateau, and call the resulting field H_s. The C^5 cutoff used in the numerical lift is not required to be smooth to all orders. Define Ψ as the time-one map of $\partial_s \Psi_s = H_s \circ \Psi_s$, $\Psi_0 = \mathrm{id}$. Smallness of d_q keeps all intermediate rigid neighborhoods in the plateau. Uniqueness of this ordinary differential equation then gives (23). The field H_s is divergence free and zero near the outer wall. The Jacobian equation gives $\det D\Psi_s = 1$.

All spatial derivatives of H_s are bounded by $C_k d_q$. Differentiating its coefficients along the physical time paths gives $\|\partial_t H_s\|_{W^{k,\infty}} \le C_k(d_q + |\widehat{q}' - q'|)$. The differentiated flow equations, Gronwall's inequality on $0 \le s \le 1$, and the backward flow yield (24)–(25). These estimates use the geometric clearance, not a regularization width. Finally, change of variables in the distributional divergence identity proves that (26) preserves solenoidality. Near the body $D\Psi = O$, and $OJ = JO$ in two dimensions, so

$$O\mathcal{R}_q(V, \omega)(x) = OV + \omega J(\Psi(x) - \widehat{c}).$$

This proves the claimed rigid trace and interior transformation. □

4.3 Recovery of a whole rigid interior

Let $q(t)$ now be any Lipschitz admissible path. Consider $\widetilde{X}(t) = (\widetilde{u}(t), \widetilde{\xi}(t)) \in \mathbb{K}(q(t))$ with $\widetilde{\xi} \in H^1_t$ and bounded speed of q. Set $w = \widetilde{u} - L_q\widetilde{\xi}$. It vanishes on the entire body, not just its boundary. Suppose $w \in H^1_t L^2_x$, its piecewise $W^{3,\infty}$ norm is uniformly bounded, and the piecewise $W^{3,\infty}$ norm of its Eulerian derivative is in L^2_t.

Lemma 4.3 (Joint common recovery)**.** *Put $\delta = 4(\bar{\varepsilon} + \sqrt{2}h)$. For small δ there is a trajectory $Z_h(t) = (z_h(t), \widetilde{\xi}(t))$ in every current joint discrete space, independent of both moment partitions and the enrichment history, for which*

$$\sup_t \|z_h - \widetilde{u}\|_U + \|\partial_t(z_h - \widetilde{u})\|_{L^2_t L^2_x} \le C\sqrt{\delta}, \qquad \sup_t \|z_h - \widetilde{u}\|_0 \le C\delta^{3/2}. \tag{27}$$

The constant depends on the displayed regularity bounds, $\|\widetilde{\xi}\|_{H^1}$, and $\|q'\|_{L^\infty}$, but on no acceleration of q.

Proof. Let $\operatorname{curl}\psi = w$, with outer clamping. Since $w = 0$ in the connected body, ψ is a scalar $c_\psi(t)$ there. With signed distance $d(t,x)$ and a smooth cutoff χ_0 equal to one on $[-1,1]$ and zero outside $[-2,2]$, set

$$\psi_\delta = \psi - \chi_0(d/\delta)(\psi - c_\psi) \quad \text{near the interface,} \qquad z_h = \operatorname{curl} I_h\psi_\delta + L_{h,q}\widetilde{\xi}.$$

The streamfunction is unchanged away from the interface tube and is constant throughout the body and the δ collar. Every coarse cell meeting the body or a regularization support lies in this constant region, possibly together with its original constant interior. Thus the centered coarse velocity is zero on the entire body and all its kernel supports. Both sets of moments therefore vanish exactly, and Lemma 4.1 completes membership.

For completeness, the width-dependent estimates are the moving collar estimates of Part II [3], and require only a Lipschitz configuration path. Writing $r = \psi - c_\psi$, one has $r = O(d^2)$, $\nabla r = O(d)$, and $r_t = O(d)$. The last assertion follows from the moving trace identity $c'_\psi = \psi_t|_{\Gamma(t)}$, since $\nabla\psi|_{\Gamma(t)} = 0$. The Eulerian derivative is

$$(\psi_\delta - \psi)_t = -\chi_0(d/\delta)r_t - \delta^{-1}\chi_0'(d/\delta)d_t r.$$

The support has area $O(\delta)$; these quadratic and linear vanishing orders give the streamfunction bounds

$$\|\psi_\delta - \psi\|_{H^2} = O(\sqrt{\delta}), \quad \|\psi_\delta - \psi\|_{H^1} = O(\delta^{3/2}), \quad \|(\psi_\delta - \psi)_t\|_{L^2_t H^1_x} = O(\sqrt{\delta}).$$

The corresponding H^4 norms of ψ_δ and $\psi_{\delta,t}$ are $O(1 + \delta^{-3/2})$ in L^∞_t and $O(1 + \delta^{-5/2})$ in L^2_t. Here $d_t = -(c' + \theta' J(x-c)) \cdot \nabla d$ has the necessary uniform spatial bounds using only q', not q''. The fixed Hermite errors in (20) are thus $h^2\delta^{-3/2}$ in the velocity H^1 norm and $h^3\delta^{-5/2}$ in the time-derivative velocity L^2 norm. Both are at most $C\sqrt{\delta}$. The lifting errors from Lemma 4.1 are smaller. This proves (27). The moving-cutoff derivative has been included explicitly; no commutation of a time-dependent recovery map with differentiation is asserted. □

Lemma 4.4 (Alignment errors at the same physical points)**.** *Suppose $u \in U$ is piecewise $W^{2,\infty}$ across $\Gamma(q)$. For small d_q,*

$$\|\mathcal{T}_\Psi u - u\|_0 \le C d_q \|u\|_{H^1}, \qquad \|\mathcal{T}_\Psi u - u\|_U \le C\sqrt{d_q}\,(\|u\|_{W^{2,\infty}(B(q))} + \|u\|_{W^{2,\infty}(F(q))}). \tag{28}$$

Proof. Integrating u along the alignment flow, whose velocity is $O(d_q)$, proves the L^2 bound; the factor $D\Psi - I$ is also $O(d_q)$. For the gradient bound, remove the Cd_q interface tube. Off this tube, an alignment trajectory remains in one smooth phase, and its gradient difference is $O(d_q)$ by the chain rule. Inside the tube, both endpoint gradients are bounded and its area is $O(d_q)$, giving the stated square-root bound. The map is the identity near the outer wall. This estimate allows a jump of the first derivatives across the fluid–rigid interface. □

5 A coupled Cartesian scheme and its exact energy law

5.1 Known geometry at each linear solve

Choose $0 = t_0 < \cdots < t_N = T$ and set $\tau_n = t_n - t_{n-1}$. Given q_0 and a compatible exact initial state X_0, initialize by the joint mass projection $X_h^0 = P_M^0 X_0$ at the pose q_0. For $n \geq 1$, first update the pose using the previous computed body velocity:

$$c_n = c_{n-1} + \tau_n V_h^{n-1}, \qquad \theta_n = \theta_{n-1} + \tau_n \omega_h^{n-1}. \tag{29}$$

The angle is represented as a real-valued continuous angle. The piecewise affine pose reconstruction has derivative $\dot{q}_h = (V_h^{n-1}, \omega_h^{n-1})$ on the nth interval. The coupled velocity solve below therefore uses a known pose, while its new body velocity determines the following pose update.

At q_n choose any admitted Cartesian enrichment, kernel width, volume-cell partition, and surface-panel partition. Write

$$\mathbb{K}_h^n = \mathbb{K}_h(q_n), \qquad P_M^n : \mathbb{H} \longrightarrow \mathbb{K}_h^n$$

for the current joint space of (16) and its orthogonal projector in (5). All the indicated parameters may change at every time step. The projection is in the combined fluid and rigid-body energy metric. The same physical bulk mass integrals are used in every configuration.

Let f^n, F_e^n, and T_e^n be approximations of the external data on the interval. The primary choice is their exact time average as ambient data; the fluid integral is taken on the *current* exterior region:

$$\mathcal{L}^n(Y) = \int_{F(q_n)} f^n(x) \cdot v(x)\, dx + F_e^n \cdot W + T_e^n \eta. \tag{30}$$

The scheme finds $X_h^n = (u_h^n, V_h^n, \omega_h^n) \in \mathbb{K}_h^n$ such that

$$\left(\frac{X_h^n - P_M^n X_h^{n-1}}{\tau_n}, Y_h \right)_M + a(u_h^n, v_h) + \mathcal{G}(\omega_h^{n-1}; X_h^n, Y_h) = \mathcal{L}^n(Y_h), \qquad Y_h \in \mathbb{K}_h^n. \tag{31}$$

The previous angular velocity is a known coefficient of a skew operator, whereas the current translational velocity is unknown in that operator. Both fluid and rigid velocities are solved together.

For a current test, orthogonality gives $(P_M^n X_h^{n-1}, Y_h)_M = (X_h^{n-1}, Y_h)_M$. Thus (31) can be assembled directly using the cross-space mass pairing with the full previous state, without performing a separate projection solve. For each admissible current geometry the linear system has a unique joint state: its bilinear form evaluated on (Y_h, Y_h) equals $\tau_n^{-1} \|Y_h\|_M^2 + a(v_h, v_h) > 0$ for $Y_h \neq 0$. The skew term does not change this coercivity. This statement is independent of the rank of the multiplier constraint matrix.

The geometric algorithm is considered until a configuration leaves the collision-free region used by the analysis. Stability below holds on every admissible prefix. The convergence argument closes the geometry bound against the assumed collision-free exact branch for sufficiently small discretization parameters; collision avoidance is not an extra conclusion of the energy identity alone.

5.2 Cancellation of the coupled reactions

Opposite fluid and structural work is the standard multiplier energy mechanism [11, 12]. Here it is applied to both regularized volume and surface moments in the same positive fluid–body mass space. Let $b_h^n(Y_h, \Lambda_h)$ be the sum of the current volume and surface moment pairings of $\mathcal{J}_{\varepsilon_n} v_h - \mathcal{R}_{q_n}(W_h, \eta_h)$ with the two multiplier components. The equivalent mixed formulation on $X_{h,\mathcal{A}^n} \times \mathbb{R}^3$ is

$$\left(\frac{X_h^n - X_h^{n-1}}{\tau_n}, Y_h\right)_M + a(u_h^n, v_h) + \mathcal{G}(\omega_h^{n-1}; X_h^n, Y_h) + b_h^n(Y_h, \Lambda_h^n) = \mathcal{L}^n(Y_h), \tag{32}$$

$$b_h^n(X_h^n, \Upsilon_h) = 0 \qquad \text{for all } \Upsilon_h.$$

The minus rigid velocity in each moment is essential: the same reaction acts with opposite fluid and body work. Testing by X_h^n annuls the entire reaction term exactly, including the interior moments. A multiplier exists because the residual of the constrained solution vanishes on the kernel of the finite-dimensional constraint map and hence belongs to the range of its transpose. It may be nonunique. No estimate of this multiplier is used in the energy or velocity-convergence arguments.

5.3 Exact identity and bounds independent of mesh history

Theorem 5.1 (Coupled discrete energy)**.** *Every step of* (31) *satisfies*

$$\|X_h^n\|_M^2 - \left\|X_h^{n-1}\right\|_M^2 + \left\|X_h^n - X_h^{n-1}\right\|_M^2 + 2\tau_n a(u_h^n, u_h^n) = 2\tau_n \mathcal{L}^n(X_h^n). \tag{33}$$

Moreover,

$$\left\|X_h^n - X_h^{n-1}\right\|_M^2 = \left\|X_h^n - P_M^n X_h^{n-1}\right\|_M^2 + \left\|(I - P_M^n) X_h^{n-1}\right\|_M^2. \tag{34}$$

Let $\ell_f^n \in U'$ denote the fluid part of (30)*, and put*

$$A_N = \sum_{n=1}^N \tau_n \left(\frac{|F_e^n|^2}{m_e} + \frac{|T_e^n|^2}{I_e}\right)^{1/2}, \qquad B_N = \left\|X_h^0\right\|_M^2 + \mu^{-1} \sum_{n=1}^N \tau_n \left\|\ell_f^n\right\|_{U'}^2.$$

Then

$$\max_{0 \le n \le N} \|X_h^n\|_M^2 + \sum_{n=1}^N \left\|X_h^n - X_h^{n-1}\right\|_M^2 + \mu \sum_{n=1}^N \tau_n \|u_h^n\|_U^2 \le C(B_N + A_N^2), \tag{35}$$

with an absolute constant C. No time-step restriction, smallness of the moment widths, bound on the number of mesh changes, or multiplier inf–sup condition is required for this estimate.

Proof. Test (31) with X_h^n. The projection may be removed inside this pairing. The skew term is zero, and the identity $2(X - Y, X)_M = \|X\|_M^2 - \|Y\|_M^2 + \|X - Y\|_M^2$ proves (33). The vector $(I - P_M^n)X_h^{n-1}$ is orthogonal to the current space, which contains $X_h^n - P_M^n X_h^{n-1}$. Pythagoras proves (34).

Write $\beta_n = (|F_e^n|^2/m_e + |T_e^n|^2/I_e)^{1/2}$. Cauchy–Schwarz in the rigid mass norm gives

$$|F_e^n \cdot V_h^n + T_e^n \omega_h^n| \le \beta_n \|X_h^n\|_M.$$

Use $a(u_h^n, u_h^n) = \mu \|u_h^n\|_U^2$ and apply Young's inequality only to the fluid work. Summing the energy identity through step k gives

$$\left\|X_h^k\right\|_M^2 + \sum_{n=1}^k \left\|X_h^n - X_h^{n-1}\right\|_M^2 + \mu \sum_{n=1}^k \tau_n \|u_h^n\|_U^2 \le B_N + 2 \sum_{n=1}^k \tau_n \beta_n \|X_h^n\|_M. \tag{36}$$

Let $Z = \max_{0\le n\le N} \|X_h^n\|_M$. If the maximum is attained at zero, $Z^2 \le B_N$. Otherwise choose a maximizing index in (36) to obtain $Z^2 \le B_N + 2A_N Z$. Hence

$$Z \le A_N + \sqrt{A_N^2 + B_N} \le 2A_N + \sqrt{B_N}.$$

Use this bound in (36) with $k = N$ to control the two accumulated nonnegative terms. This proves (35). The argument is an algebraic maximum estimate and does not introduce a time-step condition through a discrete Gronwall denominator. □

For exact ambient time averages, $\left\|\ell_f^n\right\|_{U'} \le C\,\|f^n\|_{L^2(\Omega)}$ and Jensen's inequality bounds its squared time sum by $C\,\|f\|^2_{L^2(0,T;L^2(\Omega))}$. Similarly A_N is bounded by the L^1-in-time rigid dual-mass norm of the external body load. In particular, the prescribed data and positive excess inertias give a uniform bound for $\max_n(|V_h^n| + |\omega_h^n|)$, and hence for the speed of the pose reconstruction in (29).

Corollary 5.2 (Physical constraint defects)**.** *Suppose the data bounds in Theorem 5.1 are uniform over a sequence of admissible computations. Then*

$$\left(\sum_n \tau_n \,\|u_h^n - \mathcal{R}_{q_n}\xi_h^n\|^2_{L^2(B(q_n))}\right)^{1/2} \le C(\bar\varepsilon + \bar\kappa), \tag{37}$$

$$\left(\sum_n \tau_n \,\|\gamma_{q_n} u_h^n - \mathcal{R}_{q_n}\xi_h^n\|^2_{L^2(\Gamma(q_n))}\right)^{1/2} \le C(\sqrt{\bar\varepsilon} + \sqrt{\bar\ell}). \tag{38}$$

Here bars denote the maxima of the indicated widths over the run. The surrogate-to-physical kinetic-energy discrepancy in (19) tends to zero in the weighted L^1 time sum as $\bar\varepsilon + \bar\kappa \to 0$.

Proof. The stability bound controls u_h in the weighted $L^2(U)$ norm. It also controls ξ_h uniformly by strict positivity of m_e, I_e. Thus $\sum_n \tau_n \|X_h^n\|^2_{\mathbb{V}}$ is bounded. Apply Lemma 3.1 and Proposition 3.3. □

Corollary 5.3 (Defects relative to the actual interpolated motion)**.** *Under the uniform bounds of Corollary 5.2, suppose also that the piecewise affine pose path remains in the fixed admissible configuration family. For $t \in (t_{n-1}, t_n]$, define*

$$U_h(t) = u_h^n, \qquad b_h^{\mathrm{path}}(t,x) = V_h^{n-1} + \omega_h^{n-1} J(x - c_h(t)).$$

The latter is the material velocity of the reconstructed body, because $\dot q_h = (V_h^{n-1}, \omega_h^{n-1})$. Then

$$\left(\int_0^T \left\|U_h - b_h^{\mathrm{path}}\right\|^2_{L^2(B(q_h(t)))}\, dt\right)^{1/2} \le C(\bar\varepsilon + \bar\kappa + \sqrt{\tau_{\max}}), \tag{39}$$

$$\left(\int_0^T \left\|\gamma_{q_h(t)} U_h - b_h^{\mathrm{path}}\right\|^2_{L^2(\Gamma(q_h(t)))}\, dt\right)^{1/2} \le C(\sqrt{\bar\varepsilon} + \sqrt{\bar\ell} + \sqrt{\tau_{\max}}). \tag{40}$$

The constants may depend on the uniform data bound and the fixed admissible family, but not on the mesh history. The nodal defects in (37)–(38) use the newly solved velocity ξ_h^n; the present bounds instead use the actual velocity of the affine pose path.

Proof. Let $w_n = u_h^n - L_{h,q_n}\xi_h^n$. The uniform mass bound controls all body velocities and therefore the speed of q_h. If $R_{t,n}$ is the exact rigid map from $B(q_n)$ to $B(q_h(t))$, its displacement and rotational change on bounded sets are at most $C\tau_n$. Zero extension of w_n and integration along this rigid map give

$$\|Ew_n \circ R_{t,n} - Ew_n\|_{L^2(\mathbb{R}^2)} \le C\tau_n \|w_n\|_U.$$

The corresponding H^1 norm is bounded by $C\|w_n\|_U$. A uniform multiplicative trace estimate therefore bounds the trace difference on $\Gamma(q_n)$ by $C\sqrt{\tau_n}\|w_n\|_U$, exactly as in the moving-trace argument of Part II [3]. The rigid map preserves volume and arclength. Combining these shift estimates with the current volume and surface defects bounds w_n on the interpolated body by $C(\varepsilon_n + \kappa_n + \tau_n)\|X_h^n\|_{\mathbb{V}}$, and its trace by $C(\sqrt{\varepsilon_n} + \sqrt{\ell_n} + \sqrt{\tau_n})\|X_h^n\|_{\mathbb{V}}$.

The common lift reproduces its rigid affine field on every body in the admissible family, including the intermediate body. At the same physical point its difference from the path velocity obeys

$$|L_{h,q_n}\xi_h^n - b_h^{\mathrm{path}}(t)| \le C|\xi_h^n - \xi_h^{n-1}| + C\tau_n \quad \text{on } B(q_h(t)) \cup \Gamma(q_h(t)).$$

Indeed, the first term accounts for the change of rigid velocity and the second for $|c_n - c_h(t)| \le C\tau_n$; all coefficients and body diameters are uniformly bounded. The additional lag contribution is controlled by the full joint jumps in the energy identity:

$$\sum_n \tau_n|\xi_h^n - \xi_h^{n-1}|^2 \le C\tau_{\max}\sum_n \|X_h^n - X_h^{n-1}\|_M^2 \le C\tau_{\max}.$$

Integrate over each interval, sum, and use $\sum_n \tau_n\|X_h^n\|_{\mathbb{V}}^2 \le C$. The terms of order $\tau_{\max}$ are bounded by a constant depending on T times $\sqrt{\tau_{\max}}$. This proves both assertions. □

The discrete dissipation is $2\mu\int_\Omega |D(u_h)|^2$. Interior strain can be nonzero at a finite resolution, as can the physical surface slip. The energy law alone does not prove that this interior strain vanishes; that conclusion uses the strong velocity convergence established subsequently. No physical torque is inferred from a raw discrete surface multiplier.

6 Closing the fluid, rigid-velocity, and configuration errors

The theorem is conditional on a sufficiently regular physical solution, not on convergence of numerical forces or trajectories. Geometry is an unknown of the discrete scheme. The comparison below is constructed on that computed geometry, and its discrepancy from the exact geometry is estimated together with the velocity error. The comparison and residual strategy has precedents in coupled geometry analyses [7, 10] and changing-space Stokes estimates [13]. The constructions and bounds below specify the regularized volume and surface consistency terms and the retained-coarse transfer argument needed for the present method.

6.1 Explicit assumptions on the exact branch and loads

Assume that (2)–(3) has a solution on $[0,T]$ with positive wall clearance, and extend its velocity rigidly inside the body. We assume

$$\begin{aligned} &u \in H^1(0,T;L^2(\Omega)^2), \qquad X(t) \in \mathbb{K}(q(t)), \qquad \xi \in H^1(0,T;\mathbb{R}^3),\\ &M_0 := \operatorname*{ess\,sup}_t \Big(\|u(t)\|_{W^{4,\infty}(B(q(t)))} + \|u(t)\|_{W^{4,\infty}(F(q(t)))}\Big) < \infty,\\ &M_1(t) := \|u_t(t)\|_{W^{3,\infty}(B(q(t)))} + \|u_t(t)\|_{W^{3,\infty}(F(q(t)))} \in L^2(0,T). \end{aligned} \tag{41}$$

The time derivative is Eulerian and may have different side traces. The extra spatial derivative compared with Part II is used when differentiating the configuration alignment: that derivative contains ∇u multiplied by the speed of the alignment map. Assume also

$$\begin{aligned} &f \in L^2(0,T;W^{1,\infty}(\Omega)^2), \qquad F_e, T_e \in L^2(0,T),\\ &\Lambda_B^2 := \int_0^T \|\lambda_B(t)\|_{L^2(B(q(t)))}^2 dt < \infty, \qquad \Lambda_\Gamma^2 := \int_0^T \|\lambda_\Gamma(t)\|_{L^2(\Gamma(q(t)))}^2 dt < \infty. \end{aligned} \tag{42}$$

Here F_e is vector valued. The volume reaction in (12) already has this regularity under (41). The surface-traction bound is a separate assumption on the exact solution. A mere ambient $L^2_t U'$ force would not justify the Lipschitz-in-configuration load estimate below; the stated spatial extension assumption is used.

The primary load choice is the exact ambient time average in (30). More generally, let a bar denote each ambient time average and define the data error before computing the trajectory by

$$E_L^2 = \sum_n \tau_n \left(\|f^n - \bar{f}^n\|^2_{L^2(\Omega)} + |F_e^n - \bar{F}_e^n|^2 + |T_e^n - \bar{T}_e^n|^2 \right). \tag{43}$$

If $\overline{\mathcal{L}}_n$ is the exact-average functional evaluated on $F(q_n)$, Lemma 3.2 and Poincare's inequality bound the squared time sum of $\sup_{Y_h \neq 0} |\mathcal{L}^n(Y_h) - \overline{\mathcal{L}}_n(Y_h)|/\|v_h\|_U$ by CE_L^2, uniformly on every admissible prefix. The data error is thus independent of the unknown computed geometry. Bounded E_L also implies the uniform data bounds used in Theorem 5.1. Exact time averages have $E_L = 0$. Endpoint loads are also covered: if $f \in H^1(0,T;L^2(\Omega)^2)$ and $F_e, T_e \in H^1(0,T)$, then the choices $f^n = f(t_n)$, $F_e^n = F_e(t_n)$, and $T_e^n = T_e(t_n)$ give

$$E_L \leq C\tau_{\max}(\|f_t\|_{L^2_t L^2_x} + \|F_e'\|_{L^2_t} + \|T_e'\|_{L^2_t}).$$

This follows from the fundamental theorem of calculus, Jensen's inequality, and Lemma 3.2; the fluid integral in both compared loads is on the same current domain $F(q_n)$. Write

$$r_h^2 = h + \bar{\varepsilon} + \bar{\ell} + \bar{\kappa}^2 + \tau_{\max} + E_L^2, \qquad \tau_{\max} = \max_n \tau_n. \tag{44}$$

All constants below may depend on the exact branch and the fixed physical parameters, including the strictly positive excess inertias, but not on a refinement history or on inverse regularization widths.

6.2 The mapped identity on all ambient tests

On an admissible prefix of the computation, align the exact pose to the piecewise affine computed pose using Lemma 4.2:

$$\begin{aligned} &\Psi(t) = \Psi(q(t), q_h(t)), \quad O(t) = Q(\theta_h(t) - \theta(t)), \quad A = D\Psi, \\ &\widetilde{u} = \mathcal{T}_\Psi u, \qquad \widetilde{\xi} = (OV, \omega), \qquad \widetilde{X} = (\widetilde{u}, \widetilde{\xi}), \quad d(t) = |q_h(t) - q(t)|. \end{aligned} \tag{45}$$

The norms used for poses are equivalent finite-dimensional norms. The comparison belongs to $\mathbb{K}(q_h(t))$, but its rigid velocity is not the speed of q_h. This distinction is retained in the following calculation.

Lemma 6.1 (An explicit geometric commutator)**.** *For every $Y = (v, W, \eta) \in \mathbb{V}$, the mapped state satisfies*

$$\begin{aligned} (\partial_t \widetilde{X}, Y)_M + a(\widetilde{u}, v) + \mathcal{G}(\omega; \widetilde{X}, Y) + \int_{B(q_h)} \widetilde{\lambda}_B \cdot (v - \mathcal{R}_{q_h}\zeta)\, dx \\ + \int_{\Gamma(q_h)} \widetilde{\lambda}_\Gamma \cdot (\gamma_{q_h} v - \mathcal{R}_{q_h}\zeta)\, ds \\ = \mathcal{L}(t, q_h; Y) + \mathcal{E}(t; Y), \end{aligned} \tag{46}$$

where $\zeta = (W, \eta)$ and the two reactions are rigid pushforwards of the exact reactions. Their respective L^2 norms are unchanged. There is a known $a_*(t) \in L^2(0,T)$, independent of the numerical errors, such that

$$|\mathcal{E}(t;Y)| \leq C(a_*(t)d(t) + |q_h'(t) - q'(t)|)\|Y\|_{\mathbb{V}}. \tag{47}$$

One may take a constant multiple of $1 + \|u_t(t)\|_0 + \|f(t)\|_{W^{1,\infty}} + |F_e(t)|$ for a_*.

Proof. In (13), use the inverse Piola fluid test $(\mathcal{T}_\Psi^{-1}v)(x) = A(x)^{-1}v(\Psi(x))$ and rigid test $(O^\mathsf{T}W, \eta)$. These are admissible ambient tests; they need not satisfy any exact or regularized rigidity constraint. On the body and its boundary $A = O$, and Ψ is a rigid map. The test mismatch therefore becomes $O^\mathsf{T}(v - \mathcal{R}_{q_h}\zeta) \circ \Psi$. Since area and arclength are preserved, both reaction integrals transform exactly, with $\widetilde{\lambda} \circ \Psi = O\lambda$. There is no difference of two regularized kernels in this calculation.

Put $z = \Psi_t \circ \Psi^{-1}$. Differentiating the Piola formula at a fixed physical point gives the exact fluid identity

$$\widetilde{u}_t - (A^{-\mathsf{T}}u_t) \circ \Psi^{-1} = ((A - A^{-\mathsf{T}})u_t + A_t u) \circ \Psi^{-1} - \nabla\widetilde{u}\, z. \tag{48}$$

The first term is bounded in L^2 by $Cd\|u_t\|_0$. The others are bounded by $C(d + |q_h' - q'|)\|u\|_{H^1}$, by (24)–(25). For the body mass, $(OV)_t = OV_t + O_tV$, and $O_t = (\theta_h' - \omega)JO$. The transformed excess-mass term thus differs by $m_e(O_tV) \cdot W$, which has the same bound. The angular mass term is unchanged. The gyroscopic term transforms without a remainder because $OJ = JO$:

$$(JV) \cdot O^\mathsf{T}W = (JOV) \cdot W.$$

In particular, the interior acceleration is not replaced by the acceleration of a body moving with $\widetilde{\xi}$. Directly there,

$$\partial_t\widetilde{b} - O\partial_t b \circ \Psi^{-1} = O_tV - \omega J(c_h' - OV). \tag{49}$$

This is part of (48), and is controlled by the pose and pose-speed errors; it has not been omitted.

For the viscous form, change variables using $\det A = 1$ and differentiate Av and $A^{-1}v \circ \Psi$. Each difference from the identity-map expression contains either $A - I$, $A^{-1} - I$, or DA. Their L^∞ norms are $O(d)$. Poincare's inequality therefore gives

$$|a(\mathcal{T}_\Psi u, v) - a(u, \mathcal{T}_\Psi^{-1}v)| \le Cd\|u\|_{H^1}\|v\|_{H^1}.$$

This also follows componentwise for the symmetric-gradient form; no assumption of a global H^2 velocity is needed for this bound.

The transformed fluid load is integrated on precisely $F(q_h)$, with density $(A^{-\mathsf{T}}f) \circ \Psi^{-1}$. Its difference from f is bounded in L^2 by $Cd\|f\|_{W^{1,\infty}}$. The transformed body force is OF_e, whose difference from F_e is at most $Cd|F_e|$; the torque is unchanged. Combining these identities proves (46) and (47). In particular no convergence or bounded inverse estimate for a discrete multiplier was used. □

The numerical speed is uniformly bounded by Theorem 5.1. On a sufficiently close admissible prefix, the preceding alignment consequently has bounded derivatives independent of all resolutions. Formula (48), the side regularity in (41), and the chain rule show that $\widetilde{u}$ is piecewise uniformly $W^{3,\infty}$ and its Eulerian derivative is piecewise $W^{3,\infty}$ in L^2_t. The fourth spatial derivative of u is used here in $\nabla\widetilde{u}\, z$. Moreover, $\widetilde{\xi} \in H^1_t$ with a uniform bound, since its derivative uses ξ' and $\theta_h' - \omega$, not a derivative of the numerical velocity. Lemma 4.3 therefore constructs

$$Z_h(t) = (z_h(t), \widetilde{\xi}(t)), \quad H_h(t) = \widetilde{X}(t) - Z_h(t) = (\eta_h(t), 0, 0), \quad Z_h(t_n) \in \mathbb{K}^n_h, \tag{50}$$

with the uniform estimates (27). No numerical acceleration bound enters their constants.

6.3 Consistency on the current joint space

Let $\overline{b}^{,n} = \tau_n^{-1} \int_{t_{n-1}}^{t_n} b(s)\, ds$. The following estimates compare the time-averaged identity (46) with the current geometry and the lagged gyroscopic coefficient.

Lemma 6.2 (Current-geometry residual bounds)**.** *On every sufficiently close admissible prefix there exist nonnegative k_n, s_n, independent of any desired trajectory-convergence assertion, such that*

$$\sum_n \tau_n k_n \le C, \qquad \sum_n \tau_n s_n^2 \le C r_h^2. \tag{51}$$

For $e^n = X_h^n - Z_h(t_n)$, $E_n = \|e^n\|_M^2$, and $P_n = |q_n - q(t_n)|^2$, subtraction of the comparison gives

$$\left(\frac{e^n - P_M^n e^{n-1}}{\tau_n}, Y_h \right)_M + a(e_u^n, v_h) + \mathcal{G}(\omega_h^{n-1}; e^n, Y_h) = \mathcal{R}_n(Y_h), \tag{52}$$

where, for all $Y_h = (v_h, \zeta) \in \mathbb{K}_h^n$,

$$|\mathcal{R}_n(Y_h)| \le C(\sqrt{k_n}\sqrt{E_{n-1} + P_{n-1}} + s_n)\|v_h\|_U. \tag{53}$$

Proof. Orthogonality removes the current projection inside a current test, including for the previous comparison $Z_h(t_{n-1})$. Thus its tested time difference is the ordinary difference of Z_h, with no mesh-change term. The exact residual is the sum of: the load difference; the averaged two reaction integrals; $-\overline{\mathcal{E}}^{,n}$; $(\overline{\partial_t H_h}^{,n}, Y_h)_M$; $a(\eta_h(t_n), v_h)$; $-a(\widetilde{u}(t_n) - \overline{\widetilde{u}}^{,n}, v_h)$; and the gyroscopic difference

$$\overline{\mathcal{G}(\omega; \widetilde{X}, Y_h)}^{,n} - \mathcal{G}(\omega_h^{n-1}; \widetilde{X}(t_n), Y_h). \tag{54}$$

Here the averaged load in the mapped equation uses $q_h(s)$, whereas the discrete load uses q_n.

We bound these terms explicitly. The configuration speed is uniformly bounded. A rigid shift over one interval has displacement $O(\tau_n)$. The L^2 translation estimate for H^1 fields on a body gives

$$\|v_h - \mathcal{R}_{q_h(s)}\zeta\|_{L^2(B(q_h(s)))} \le C(\varepsilon_n + \kappa_n + \tau_n)\|Y_h\|_{\mathbb{V}}. \tag{55}$$

Indeed, pull the integral back by the rigid map from $B(q_n)$: the difference of the pulled field and v_h is bounded by $C\tau_n\|v_h\|_{H^1}$ by integration along the rigid path, and the difference of the two affine rigid test fields is $C\tau_n|\zeta|$. The remaining term is (17). The analogous surface estimate is

$$\|\gamma_{q_h(s)} v_h - \mathcal{R}_{q_h(s)}\zeta\|_{L^2(\Gamma(q_h(s)))} \le C(\sqrt{\varepsilon_n} + \sqrt{\ell_n} + \sqrt{\tau_n})\|Y_h\|_{\mathbb{V}}. \tag{56}$$

For the shifted trace, integration on normal fibers gives a $C\sqrt{\tau_n}\|v_h\|_{H^1}$ bound, and the tangential change of parametrization is controlled by its $H^{1/2}$ trace seminorm. Equivalently one may use the rigid-pullback trace estimate proved in Part II [3]. The normal and tangential maps have uniform Jacobians on this admissible family. Applying (18) proves (56). Pairing with the two mapped reactions and Jensen's inequality gives total squared residual at most

$$C(\bar{\varepsilon} + \bar{\kappa} + \tau_{\max})^2 \Lambda_B^2 + C(\bar{\varepsilon} + \bar{\ell} + \tau_{\max})\Lambda_\Gamma^2.$$

Thus time averaging never replaces a reaction on one configuration by a reaction on another without a displacement estimate.

The symmetric difference of $F(q_h(s))$ and $F(q_n)$ has area $O(\tau_n)$. Therefore the current-domain load discrepancy is at most $C\sqrt{\tau_n}\|f(s)\|_{L^\infty}\|v_h\|_0$. Its squared time sum is bounded by $C\tau_{\max}\|f\|_{L_t^2 L_x^\infty}^2$, in addition to E_L^2. The comparison derivative and spatial errors contribute

at most $C\delta$ to that sum by (27). For the viscous endpoint/average term, the swept-strip proof of Part II gives

$$\|\widetilde{u}(t)-\widetilde{u}(s)\|_U \le C\sqrt{|t-s|}+C\int_s^t \|\widetilde{u}_r\|_{W^{3,\infty}(B(q_h(r)))\oplus W^{3,\infty}(F(q_h(r)))}\,dr.$$

The strip has area $O(|t-s|)$ and gradients are bounded; away from it, integrate the side derivative. Jensen's inequality then gives a squared time sum bounded by $C\tau_{\max}$.

To close the geometric residual rather than assume it small, on $s\in[t_{n-1},t_n]$ use

$$\begin{aligned} d(s) &\le \sqrt{P_{n-1}}+C\tau_n,\\ |q_h'(s)-q'(s)| &\le C\sqrt{E_{n-1}}+C\sqrt{P_{n-1}}+|\xi(s)-\xi(t_{n-1})|. \end{aligned} \tag{57}$$

The second line uses $\widetilde{\xi}(t_{n-1})=(O(t_{n-1})V(t_{n-1}),\omega(t_{n-1}))$ and $q_h'=\xi_h^{n-1}$. It does not use a derivative of ξ_h. Equations (47) and (57) imply the past-error contribution in (53) with $k_n=C(1+\overline{a_*^2}^{,n})$. The remaining terms have squared time sum $C\tau_{\max}^2(\|a_*\|_{L^2}^2+\|\xi'\|_{L^2}^2)$.

Finally, split (54) at $\mathcal{G}(\omega(t_n);\widetilde{X}(t_n),Y_h)$. Its time-variation part has squared time sum $C\tau_{\max}^2$ because ω and $\widetilde{\xi}$ have uniform H_t^1 bounds. The remaining coefficient obeys

$$|\omega(t_n)-\omega_h^{n-1}|\le C\sqrt{E_{n-1}}+|\omega(t_n)-\omega(t_{n-1})|.$$

The last term again contributes at most $C\tau_{\max}^2\|\omega'\|_{L^2}^2$ to the squared time sum. Throughout, Lemma 3.2 replaces $\|Y_h\|_{\mathbb{V}}$ by $C\|v_h\|_U$ for small $\bar{\kappa}$. Collecting the displayed bounds proves (51)–(53). □

6.4 The coupled recursion and its consequence

Theorem 6.3 (Conditional convergence with an unknown trajectory)**.** *Assume (4), the stated body and partition regularity, and (41)– (42). Initialize with the exact pose $q_0=q(0)$ and $X_h^0=P_M^0X(0)$. For all sufficiently small r_h, the numerical configurations remain in a collision-free neighborhood of the exact branch through time T, and the scheme is defined there. One has*

$$\begin{aligned} &\max_n(|q_n-q(t_n)|+|\xi_h^n-\xi(t_n)|+\|u_h^n-u(t_n)\|_0)\\ &\quad+\left(\sum_n \tau_n\|u_h^n-\mathcal{T}_{\Psi(t_n)}u(t_n)\|_U^2\right)^{1/2}\le Cr_h. \end{aligned} \tag{58}$$

The same-point physical energy seminorm satisfies the generally weaker estimate

$$\left(\sum_n \tau_n\|u_h^n-u(t_n)\|_U^2\right)^{1/2}\le C(r_h+\sqrt{r_h}). \tag{59}$$

In particular it converges strongly. No ratio between the time step, mesh size, and regularization widths is required, and there is no factor counting enrichment changes. The theorem gives no multiplier or force convergence estimate.

Proof. Test (52) by e^n. Its skew term is zero. Projection orthogonality and polarization give

$$E_n-E_{n-1}+\|e^n-e^{n-1}\|_M^2+2\mu\tau_n\|e_u^n\|_U^2=2\tau_n\mathcal{R}_n(e^n).$$

Use (53) and Young's inequality to absorb one viscous term. After changing constants,

$$E_n-E_{n-1}+\|e^n-e^{n-1}\|_M^2+\mu\tau_n\|e_u^n\|_U^2\le C\tau_nk_n(E_{n-1}+P_{n-1})+C\tau_ns_n^2. \tag{60}$$

All error terms on the right are from the previous step. In particular the lagged gyroscopic coefficient leaves no current error term: $\mathcal{G}(\omega_h^{n-1}; e^n, e^n) = 0$.

The exact kinematic truncation defect is

$$r_q^n = q(t_n) - q(t_{n-1}) - \tau_n \xi(t_{n-1}), \qquad \sum_n \frac{|r_q^n|^2}{\tau_n} \le \tau_{\max}^2 \|\xi'\|_{L^2(0,T)}^2.$$

Subtracting the exact pose increment from (29) and using $|\xi_h^{n-1} - \xi(t_{n-1})| \le C\sqrt{E_{n-1}} + C\sqrt{P_{n-1}}$ gives, for $\tau_n \le 1$,

$$P_n \le (1 + C\tau_n) P_{n-1} + C\tau_n E_{n-1} + C\tau_n^{-1} |r_q^n|^2. \tag{61}$$

This is simply Young's inequality applied to the pose increment; it does not assume that the computed path is already convergent.

Set $A_n = E_n + P_n$ and enlarge k_n by a fixed constant if needed. Combining the two recursions yields

$$A_n + \|e^n - e^{n-1}\|_M^2 + \mu\tau_n \|e_u^n\|_U^2 \le (1 + C\tau_n k_n) A_{n-1} + C\tau_n s_n^2 + C\tau_n^{-1} |r_q^n|^2. \tag{62}$$

Iteration uses $\prod_j (1 + C\tau_j k_j) \le \exp(C \sum_j \tau_j k_j)$. The sum in the exponent is uniformly bounded by (51), even though its individual coefficients need not be uniformly bounded. Applying the same argument after adding the accumulated nonnegative increment and viscous terms gives

$$\max_n A_n + \sum_n \|e^n - e^{n-1}\|_M^2 + \mu \sum_n \tau_n \|e_u^n\|_U^2 \le C(A_0 + r_h^2). \tag{63}$$

At initialization the poses agree and $\Psi(0) = \mathrm{id}$. Since $Z_h(0) \in \mathbb{K}_h^0$, $e^0 = P_M^0(X(0) - Z_h(0))$. The best-approximation property and the recovery bound therefore give $A_0 \le C\delta^3 \le C r_h^2$.

The argument has so far been made on a sufficiently close admissible prefix, to justify the alignment. Choose two nested pose neighborhoods of the exact branch, with positive clearance on the larger one. The energy bound supplies a fixed bound for each numerical pose increment. For small $\tau_{\max}$, a first exit from the smaller neighborhood still lies in the larger one. All preceding constants are uniform there, so (63) makes the pose error smaller than half the exit threshold when r_h is sufficiently small, a contradiction. This continuation argument extends the estimate through T and proves that the linear solve always uses an admissible geometry. Its smallness threshold depends on the exact collision-free branch, not on a ratio of numerical parameters.

The recovery bound now gives the aligned fluid energy estimate. The rigid error satisfies $|\xi_h^n - \xi(t_n)| \le C\|e^n\|_M + C\sqrt{P_n}$. Lemma 4.4 gives the same-point bulk L^2 estimate, proving (58). Its U estimate gives

$$\left(\sum_n \tau_n \|\mathcal{T}_{\Psi(t_n)} u(t_n) - u(t_n)\|_U^2 \right)^{1/2} \le C \big(\max_n |q_n - q(t_n)| \big)^{1/2},$$

which proves (59). □

Corollary 6.4 (Recovery of physical interior inertia and dissipation)**.** *Under Theorem 6.3,*

$$\max_n \|u_h^n - \mathcal{R}_{q_n} \xi_h^n\|_{L^2(B(q_n))} \le C r_h, \qquad \sum_n \tau_n \|D(u_h^n)\|_{L^2(B(q_n))}^2 \le C r_h^2.$$

The nodal surrogate-to-physical kinetic-energy difference is at most $C r_h$ uniformly in time.

Proof. The aligned exact velocity equals $\mathcal{R}_{q_n}\widetilde{\xi}(t_n)$ in $B(q_n)$ and has zero strain there. The mass error and recovery bounds control the first displayed difference, including $|\xi_h^n - \widetilde{\xi}(t_n)|$; the aligned energy estimate controls the interior strain. Finally apply the factorization (19) and the uniform discrete mass bound. Unlike the time-integrated statement obtained from constraints alone, this nodal assertion uses the convergence theorem. □

Corollary 6.5 (Vanishing joint transfer losses)**.** *Under Theorem 6.3,*

$$\begin{aligned}\sum_n (\|X_h^n - P_M^n X_h^{n-1}\|_M^2 + \|(I - P_M^n)X_h^{n-1}\|_M^2) \\ = \sum_n \|X_h^n - X_h^{n-1}\|_M^2 \le C r_h^2.\end{aligned} \tag{64}$$

Thus neither the accumulated transfer loss nor the accumulated implicit-step increment loss survives the convergence limit.

Proof. The increment term retained in (63) controls $\sum_n \|e^n - e^{n-1}\|_M^2$ by Cr_h^2. The mapped state has a uniform $H_t^1\mathbb{H}$ bound, and (27) gives the same bound for Z_h. Consequently

$$\sum_n \|Z_h(t_n) - Z_h(t_{n-1})\|_M^2 \le \tau_{\max}\|\partial_t Z_h\|_{L_t^2 M}^2 \le C\tau_{\max}.$$

Use $X_h^n = e^n + Z_h(t_n)$ and $\tau_{\max} \le r_h^2$. The equality is the orthogonal splitting (34). No bound on the number of changes of the joint constraint space is used. □

For the piecewise constant velocity reconstruction and the piecewise affine pose, the same convergence conclusions hold on $[0, T]$. The exact velocity is $H_t^1 L_x^2$, and the swept-strip argument gives its U time modulus of order $\sqrt{|t-s|}$ plus the integral of its side time-derivative norm. These add at most $C\sqrt{\tau_{\max}}$ to the displayed bounds. Thus the theorem includes strong convergence of the physical Eulerian velocity in $L^2(0, T; H^1(\Omega)^2)$. If an additional global $L_t^\infty H_x^2$ bound is available, the second alignment bound is Lipschitz in the pose, and the physical energy rate improves to Cr_h. Without that extra regularity, claiming the aligned rate for the same-point H^1 error would ignore the displaced jump in the velocity gradient.

7 Minimal verification with an unknown body trajectory

The computations test the coupled implementation, the energy identity, and the response of a freely computed rigid body. They are deliberately small manufactured-solution tests in the sense of Salari and Knupp [39]; they do not constitute an asymptotic-rate study or a validation against experimental fluid–structure data. In particular, the reference trajectory below is never assigned during time stepping. All poses after initialization are obtained from the preceding computed body velocity through (29).

7.1 A continuous Stokes–Newton manufactured solution

The reference body is an ellipse with semiaxes $a = 0.19$ and $b = 0.115$, in $\Omega = (0, 1)^2$. Set $T = 0.5$, $\rho_f = 1$, $\rho_s = 4$, and $\mu = 0.1$. The homogeneous solid has

$$m_s = 4\pi ab, \qquad I_s = \pi ab(a^2 + b^2), \qquad m_e = 3\pi ab, \qquad I_e = \frac{3\pi ab(a^2 + b^2)}{4}.$$

Thus $m_e \simeq 0.2059314$ and $I_e \simeq 0.002539392$ are strictly positive. For constructing continuous data and measuring errors, choose

$$\begin{aligned} c_*(t) &= (0.5 + 0.04\sin(2t),\ 0.5 + 0.03\sin(3t)), \\ V_*(t) &= (0.08\cos(2t),\ 0.09\cos(3t)), \\ \theta_*(t) &= 0.6\sin(2t), \qquad \omega_*(t) = 1.2\cos(2t). \end{aligned} \tag{65}$$

A star denotes the reference solution, not an input to the numerical pose update. With $z = Q(\theta_*)^{\mathsf{T}}(x - c_*)$, define

$$\phi(t,x) = z_1^2/a^2 + z_2^2/b^2 - 1, \qquad W(x) = x_1^2(1-x_1)^2 x_2^2(1-x_2)^2, \qquad \alpha(t) = 0.3 + 0.2\sin(2t).$$

We use $\operatorname{curl}\psi = (\partial_2\psi, -\partial_1\psi)$ and set

$$u_*(t,x) = g_*(t,x) + \operatorname{curl}\{\alpha(t)W(x)[\phi(t,x)]_+^2\}, \qquad p_* = 0. \tag{66}$$

The fixed-cutoff rigid lift is

$$\begin{aligned} g_* &= \operatorname{curl}\left[\chi(x)\left\{\beta_{*,1}X_2 - \beta_{*,2}X_1 - \tfrac{1}{2}\omega_*|X|^2\right\}\right], \\ X &= x - (0.5, 0.5), \qquad \beta_* = V_* - \omega_* J(c_* - (0.5, 0.5)). \end{aligned}$$

The radial cutoff equals one for $|X| \le 0.40$ and zero for $|X| \ge 0.49$. In the intervening annulus it is

$$\chi = 1 - 2772\int_0^s r^5(1-r)^5\,dr, \qquad s = \frac{|X|^2 - 0.40^2}{0.49^2 - 0.40^2}.$$

This cutoff is C^5. It covers the body, the kernel supports and the coarse interpolation cells for every computed configuration in the archive; the code checks a conservative bound at every step. The velocity is divergence free, vanishes on the outer wall, and is rigid inside the exact body. The power two in (66) retains nonzero exterior shear at the interface. In particular, this is not a zero-traction manufactured test.

The exterior force is constructed from the smooth ambient field

$$\widetilde{u}_*(t,x) = g_*(t,x) + \operatorname{curl}\{\alpha(t)W(x)\phi(t,x)^2\}, \qquad f = \rho_f\partial_t\widetilde{u}_* - \mu\Delta\widetilde{u}_*. \tag{67}$$

The positive-part operation is absent from this ambient extension. In every discrete load integral, $f(t_n, x)$ is restricted to the *computed* exterior $F(q_h^n)$. This distinction matters when the computed and reference bodies do not coincide: clipping the applied force to the reference exterior would define a different method and would not give the smooth ambient data assumed in the analysis. No manufactured reference acceleration is inserted as an interior fluid load.

On the exact interface, $n_* = \nabla\phi/|\nabla\phi|$ and direct stress evaluation yields

$$\sigma_* n_* = -2\mu\alpha W|\nabla\phi|^2 J n_*. \tag{68}$$

The external body data are the continuous physical Newton loads

$$F_e = m_s\dot{V}_* - \int_{\Gamma(q_*)}\sigma_* n_*\,ds, \qquad T_e = I_s\dot{\omega}_* - \int_{\Gamma(q_*)} J(x - c_*)\cdot\sigma_* n_*\,ds.$$

They depend on time alone and are evaluated without numerical fluid coefficients. The stress integrals use 128 equally spaced angular points; the parametrized integrands reduce to smooth trigonometric polynomials and the reported independent stress checks agree to roundoff. The fluid and body forcing therefore come from a continuous PDE–ODE solution, rather than from a discrete matrix residual. Endpoint evaluation of these data is an approximation of the temporal load in (43); it contributes a load consistency error and is not identified with exact time averaging.

7.2 Discrete constraints, transfer and diagnostics

The coarse Cartesian spacing is $h = 1/M$. The complete clamped bicubic Hermite stream-function space is retained, and selected cells receive four center Hermite enrichment modes on their four half-cells. The resulting velocity space is conforming and exactly divergence free. Selection follows a narrow ring around the computed ellipse and alternates between its left and right sides each step. This changes the active space while keeping its coarse subspace. The kernel is a nonnegative, symmetric tensor-product smooth bump with support radius bounded by $\varepsilon = h/2$. Each one-dimensional kernel quadrature is split symmetrically at Cartesian polynomial breakpoints and normalized to unit mass, preserving its zero first moment. The surface partition has equal angular panels, with panel count equal to the ceiling of ellipse perimeter divided by h. For the interior moments, we intersect the reference ellipse with Cartesian squares of side h, retain every positive-area intersection, and transport these cells by the computed rigid motion. Thus the cell diameter is at most $\sqrt{2}h$, even for small cut cells.

Both constraint families are assembled as $C(q_h^n)u_h^n - R(q_h^n)\xi_h^n = 0$. Their right-hand rigid averages use the same positive quadrature as their fluid counterparts. The coarse rigid lifting modes consequently satisfy the assembled constraints to roundoff. Surface and volume constraints are not replaced by pointwise no-slip or exact interior rigidity. Their remaining physical defects are measured separately. The linear joint step includes the skew translational block $m_f\omega_h^{n-1}J$ and uses the full previous state in the constant mass pairing. A row-space singular value decomposition removes algebraic redundancy; the relative rank tolerance is 10^{-12}. The resulting nonsymmetric Schur system is solved by LU factorization. The initial state is a joint M-orthogonal projection of $(u_*(0), \xi_*(0))$, with exact initial pose. For example, at $M = 24$ this projection changes the initial body velocity by 1.10×10^{-3} in its three-component Euclidean norm; fixing it back to the reference value would change the initialization.

Mass and stiffness integrals are polynomial-exact with four-point Gauss rules on Cartesian half-cells. The default kernel, surface, volume, regular-load, curved-cut-load and sharp-trace rules have orders $6, 4, 4, 6, 10, 10$, respectively. The stronger-quadrature control raises these to $10, 8, 6, 10, 16, 16$. Curved load integration is split at exact conic intersections, including the moving computed ellipse. The interior-defect diagnostic uses a separate order-eight rule (order twelve in the stronger control). It is not used to impose the constraints or solve the equations.

The reported final fluid errors compare $u_h(T)$ and $u_*(T)$ at the same physical points in the whole box, with the reference rigid extension inside $B(q_*(T))$. Their relative denominators are the corresponding exact fluid norms. They are *unaligned* diagnostics, not the geometry-aligned error in (58). Body position, angle, translation-velocity and angular-velocity errors are absolute. We also record the physical defects

$$S^2 = \sum_n \tau \left\| u_h^n - \mathcal{R}_{q_h^n}\xi_h^n \right\|^2_{L^2(\Gamma(q_h^n))}, \qquad D^2 = \sum_n \tau \left\| u_h^n - \mathcal{R}_{q_h^n}\xi_h^n \right\|^2_{L^2(B(q_h^n))}.$$

These are nodal sums, not exact continuous-time integrals. Sharp surface traces are integrated after splitting the ellipse at all Cartesian polynomial crossings. A separate order-eight versus order-sixteen interior integration at the same saved $M = 24$ final state changes its rigidity norm by relative 3.02×10^{-4}. This diagnostic check does not constitute a quadrature-error theorem.

7.3 Refinement and controlled changes

The archive contains eight runs. The three spatial cases use $M = 12, 24, 48$, $N = 80$, and $\tau = T/N = 0.00625$, with an active-space change at every step. Four controls start from the $M = 24$ case: a half time step ($N = 160$); a genuinely fixed active Cartesian basis while the

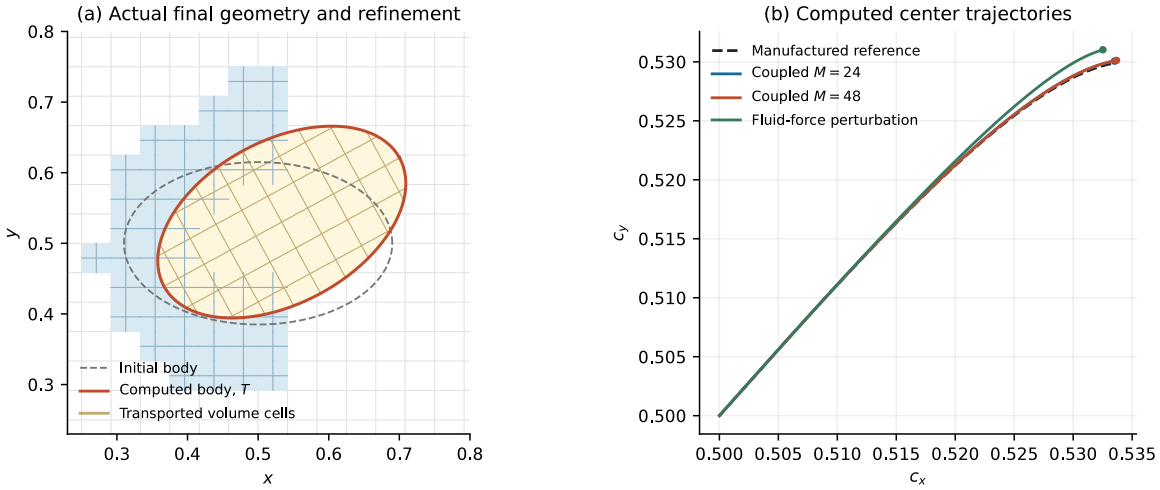

Figure 1: A computed translating and rotating body. Left: the final $M = 24$ manufactured case, showing the actual enriched Cartesian region and transported interior cells; the dashed ellipse is the initial body. Right: computed center trajectories. The perturbed case receives an additional fluid load with unchanged body loads.

M	Fluid L^2 (%)	$\lvert c_h - c\rvert$	$\lvert\theta_h - \theta\rvert$	$\lvert V_h - V\rvert$	$\lvert\omega_h - \omega\rvert$
12	49.600	2.15×10^{-3}	3.56×10^{-2}	2.65×10^{-3}	9.33×10^{-2}
24	12.696	2.11×10^{-4}	6.16×10^{-3}	6.32×10^{-4}	2.13×10^{-2}
48	1.999	1.99×10^{-4}	3.43×10^{-3}	2.90×10^{-4}	1.36×10^{-2}

Table 1: Errors at $T = 0.5$ for the coupled manufactured solution, with $N = 80$ and dynamic refinement at every step. The fluid column is a percentage; all rigid-body columns are absolute errors.

body and all constraint geometries still move; stronger quadrature; and a perturbation of the fluid forcing only. The eighth run turns off both fluid and body external loads. All runs maintain positive wall clearance.

Table 1 and Figure 2 show decreasing fluid errors and interior/surface defects. The coarsest fluid error is substantial; the narrow fixed lift transition is only poorly resolved at $M = 12$. The position error levels off between $M = 24$ and 48 at the fixed time step. We infer neither an asymptotic spatial rate nor a dominant error source from these three resolutions. In the $M = 24$ half-step control, the position error decreases while the angle error increases; finite-resolution cancellation is possible. One temporal control does not establish a temporal order or monotone convergence of all body components.

Control	Relative fluid L^2	Δc	ΔV	$\Delta\omega$
Fixed active basis	2.00×10^{-4}	4.15×10^{-5}	1.27×10^{-4}	5.81×10^{-4}
Half time step	2.47×10^{-4}	8.87×10^{-5}	1.07×10^{-4}	8.70×10^{-4}
Stronger quadrature	5.90×10^{-5}	1.37×10^{-6}	3.38×10^{-6}	1.49×10^{-5}
Fluid-force perturbation	4.55×10^{-2}	1.37×10^{-3}	5.25×10^{-3}	1.58×10^{-1}

Table 2: Changes from the dynamic $M = 24$, $N = 80$ baseline at T. The first column of values is the fluid difference divided by the baseline fluid L^2 norm; the remaining columns are absolute differences in position and rigid velocities. The last row measures a physical forcing response, not an exact-solution error.

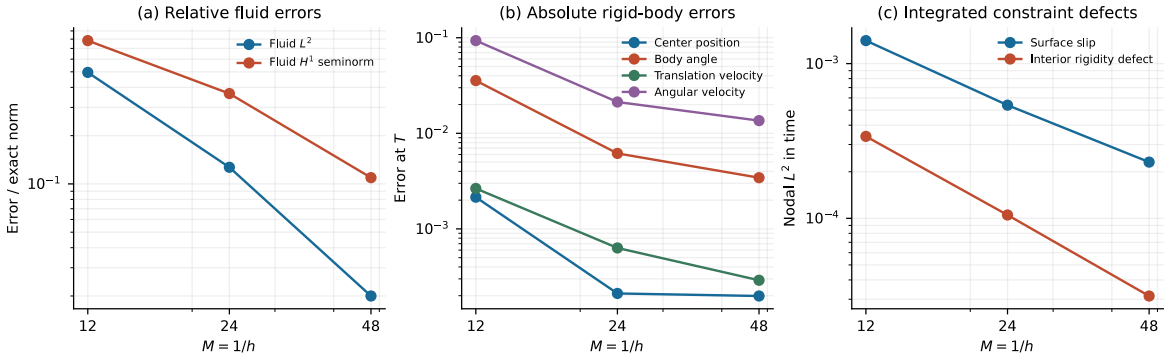

Figure 2: Finite-resolution observations at fixed $N = 80$. The fluid errors are measured without geometry alignment. The distinct body components and nonzero moment defects are retained; no fitted asymptotic slope is asserted.

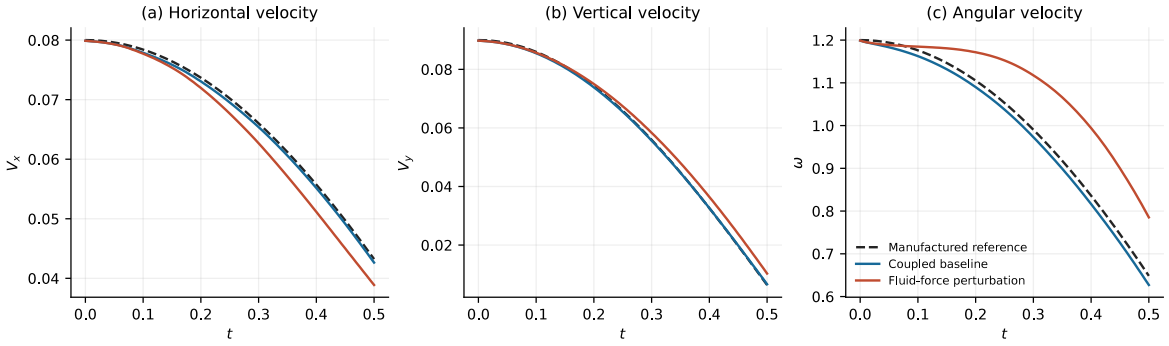

Figure 3: Computed body velocities with unchanged external body force and torque but a changed fluid load. The dashed curve is the manufactured reference for the baseline problem only; it is not an exact solution for the perturbed problem.

The fixed-active-basis run has exactly zero mesh changes; it still uses the computed moving volume and surface moments. The stronger-quadrature control changes the final fluid velocity by relative 5.90×10^{-5}. These comparisons isolate useful implementation sensitivities but do not prove that the default quadrature error is negligible in every norm. For the feedback test we add only

$$\Delta f(t, x) = 30 \sin(\pi t/T) \operatorname{curl} W(x)$$

to the ambient fluid force, again integrated over the computed exterior, and leave F_e, T_e unchanged. The final body center changes by 1.37×10^{-3} and its angular velocity by 1.58×10^{-1} from baseline. Figure 3 displays this response. It provides a direct check that the trajectory is a coupled unknown: changing only fluid forcing changes body motion. No exact-solution errors are reported for this perturbed problem or for the unforced problem.

7.4 Energy and independent implementation audits

For the unforced run, the discrete joint energy decreases from 4.23×10^{-1} to 3.80×10^{-5} with no positive nodal increment. Figure 4 plots this energy, the separately estimated physical energy, and the transfer loss. The exact algebraic identity concerns $\frac{1}{2} \|X_h^n\|_M^2$; the physical energy estimate subtracts interior fluid kinetic energy and adds full solid kinetic energy. They are not identified at finite resolution. Across the eight runs the largest sampled gap is 1.59×10^{-6}, with the accuracy of the interior integral subject to the stated diagnostic quadrature.

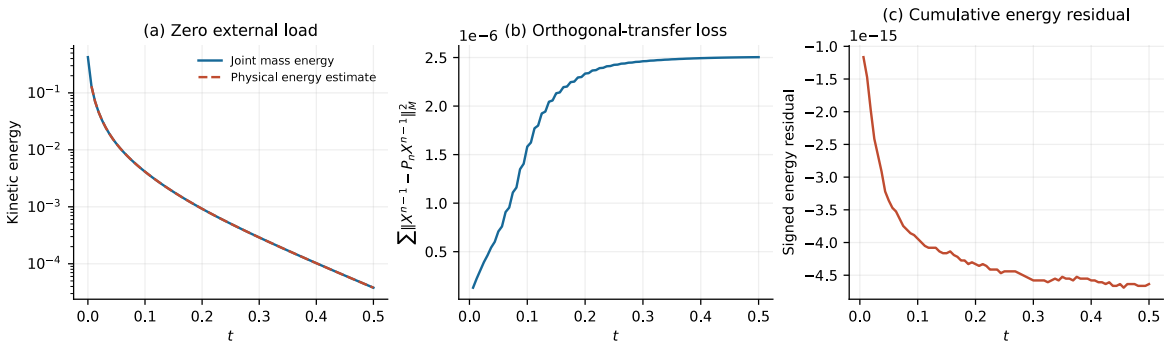

Figure 4: Unforced coupled dynamics under repeated space changes. Joint energy decreases; the physical-energy estimate is visually close but has a different finite-resolution definition. Orthogonal projection removes energy, and the cumulative balance closes to floating-point accuracy.

The maximum absolute per-step energy residual is 1.15×10^{-14} and the maximum cumulative balance residual is 2.13×10^{-13}. The latter checks

$$E_h^n - E_h^0 + \sum_{j=1}^{n} \tau a(u_h^j, u_h^j) + \frac{1}{2}\sum_{j=1}^{n} \left\| X_h^j - X_h^{j-1} \right\|_M^2 - \sum_{j=1}^{n} \tau \mathcal{L}_h^j(X_h^j) = 0.$$

The maximum gyro power is 1.05×10^{-19}, the assembled constraint residual is 4.39×10^{-15}, the common-lift feasibility residual is 5.94×10^{-14}, and the joint projection jump-split residual is 2.78×10^{-17}. The saved body states also satisfy the computed-pose recurrence with maximum absolute residual 5.55×10^{-17}. These are algebraic and implementation checks, not estimates of PDE truncation error.

Three standalone audit programs supplement the saved-state audit. First, exterior stresses reconstructed directly from analytic velocity gradients recover (68); independent interior integration recovers the Eulerian fictitious-inertia correction, physical Newton balance, and zero rigid Reynolds energy flux. Second, a small joint step agrees with a direct dense mixed-system solve to relative 1.35×10^{-14} and satisfies joint projection Pythagoras. That projection preserves the mass pairings with the current cutoff rigid test modes; this is not asserted to be global physical momentum conservation in a bounded no-slip box. Third, an intentionally offset computed body gives quadrature points inside the reference body but outside the computed body. The ambient force there is checked against the smooth exterior formula and its time derivative, demonstrating that reference-body clipping is absent. The archive contains all input configurations, final coefficients, computed pose and velocity histories, energy terms, independent audit reports, and scripts that regenerate every table and figure.

8 Relation to the prescribed-motion framework and limitations

The present construction shares the background Stokes operator, retained Cartesian coarse space, regularized moment enforcement, orthogonal transfer, and moving-collar recovery with Parts I–II. Its continuous model reduces to prescribed motion when the rigid trajectory is supplied externally. The *discrete* construction has an additional ingredient: volume moments are needed to recover the physical rigid interior when its acceleration is unknown. Freezing the body velocities therefore gives an interior-completed prescribed-motion method, not literally the surface-only scheme of Part II. This distinction prevents an incorrect assertion that surface no-slip alone legitimizes subtracting displaced-fluid mass.

The positive excess-mass restrictions make the ambient kinetic form an inner product on independent fluid and rigid variables. They permit a current-space orthogonal projector with constants independent of regularization and mesh history. The physical energy of an exact rigid interior can remain positive outside this parameter regime; the present restriction is a property of the chosen proof and discrete ambient formulation. Our constants may depend on inverse excess mass and inertia. They provide no uniform statement as either quantity approaches zero.

The state-space energy is an exact discrete identity. At finite resolution it includes interior fluid motion that is only approximately rigid. Proposition 3.3 quantifies its difference from the physical exterior-fluid and rigid-body kinetic energy. Conversely, the gyroscopic correction is invisible to that energy identity: it performs zero work. Energy tests alone cannot detect its omission. The momentum equations and the independent manufactured-force audit are consequently necessary parts of verification.

The numerical geometry is genuinely computed. The proof does not assume that it equals the exact trajectory, nor does it assume convergence of a surface multiplier to infer the body acceleration. Instead, interior and surface reactions enter through consistency defects of coupled test functions, and an alignment map compares the two configurations. The mapping is used only in the analysis; the Eulerian mesh is not transported. The discrete geometry update and lagged angular coefficient are specified parts of the algorithm, not an unresolved nonlinear monolithic solve.

A smooth exact solution with a positive clearance is assumed on the interval of interest. This paper does not prove existence of that solution for arbitrary weak data or establish a collision law. The convergence argument controls the computed clearance by closeness to that exact configuration. It also requires the stated spatial regularity of an ambient extension of the fluid load. An arbitrary load discontinuity across a separately prescribed moving surface would require additional geometric consistency analysis.

Geometry-aligned energy convergence and same-point Eulerian energy convergence answer different questions. A small displacement of an interface across which the velocity gradient jumps produces a strip of gradient mismatch. Its L^2 size is generally proportional to the square root of the displacement. Consequently, a weaker same-point energy bound does not show that the time integrator or body trajectory has that weaker order. Nor do the upper bounds assert sharp rates for all smooth data.

All theoretical constraints, kernels, and integrals are exact. The computations use quadrature and finite-precision linear algebra; they verify selected behavior and report those additional errors. There is no pressure estimate, full multiplier convergence theorem, adaptive marking result, or adaptive optimality result. The refined patch may change arbitrarily, but refinement of the retained coarse grid is part of the limiting sequence. Multiple bodies, general Navier–Stokes convection, and lighter-body ambient formulations require further analysis.

9 Machine-checked algebra and scope of verification

The accompanying Lean project contains 48 kernel-checked theorems: 35 unchanged declarations inherited from Part II and 13 additions for the coupled formulation. The complete project was compiled with Lean 4.19.0 and a pinned Mathlib revision. The six proof modules were then checked separately and their axiom dependencies printed. Every declaration passed; the reported foundations are only `propext`, `Classical.choice`, and `Quot.sound`. There are no proof admissions or custom axioms. The compiler output, dependency lockfile, source hashes, and exact commands are included in the repository. Lean and Mathlib provide the verification framework [40, 41].

The nine additions in `Coupled.lean` construct a genuine Hilbert product using square-root mass coordinates, identify its inner product and squared norm, and prove positive definiteness under positive excess mass and inertia. The fluid Hilbert norm may already contain ρ_f; a separate checked identity makes the explicit encoding $(\sqrt{\rho_f}\,u, \sqrt{m_e}\,V, \sqrt{I_e}\,\omega)$ and all three coefficients of (5) visible. The module also checks the exact step and cumulative energy identities with Mathlib's actual orthogonal projector, the zero work of the planar quarter-turn, and reaction-power cancellation using genuine adjoint operators. At finite resolution the resulting positive norm is the discrete energy surrogate; its identification with physical energy requires the analytical interior-rigidity argument.

The four additions in `Recurrence.lean` combine energy and pose-error inequalities and establish a discrete Gronwall estimate with cumulative dissipation and the factor $\exp(\sum_n \gamma_n)$. The nonnegative growth coefficients need not have a uniformly bounded maximum. Their analytic bounds and the consistency residuals are explicit hypotheses. A vector estimate for the lagged kinematic update is checked with the stated normalization $0 < \tau_n \leq 1$; this normalization belongs to that error estimate, not to the unrestricted discrete energy identity.

These checks establish the indicated algebra and finite-sum arguments, not a formal proof of the full PDE convergence theorem. The physical Eulerian inertia derivation, regularized volume and surface estimates, pose alignment, moving-collar recovery, regularity assumptions, and clearance bootstrap remain ordinary mathematical proofs. In particular, zero gyroscopic work does not prove that the gyroscopic coefficient has been derived correctly from the physical equations. The numerical checks supply a further, finite-resolution assessment of the implemented scheme; neither compiler acceptance nor those computations replace the analytical hypotheses of the convergence theorem.

AI use, human understanding, and verification limits

The research direction, scope, and revision requests were provided by Sida He. OpenAI ChatGPT/Codex agents generated most of the mathematical derivations, manuscript text, numerical implementation, and Lean formalization, and performed automated literature searches and internal checks. This work is therefore disclosed as primarily AI-generated text, rather than merely language editing.

At the preparation date of this version, the author reports that he does not understand the mathematical proofs and has not independently verified them. The intended Hexagon disclosure is *Human understanding: no parts*, with respect to the proofs. No independent human expert verification or external peer review of the proofs is claimed. Internal reviews by additional AI agents do not constitute independent human mathematical review.

The Lean checks described above cover selected algebraic identities and finite-step arguments only. They do not formalize the full PDE convergence theorems or establish their analytic hypotheses. Numerical experiments are implementation checks and illustrations, not proofs. The original proof source, dependency pins, numerical results, and recorded build logs are retained in the companion reproducibility material. This preparation revision does not claim a new Lean compilation or a new numerical experiment. The manuscript is offered for critical scrutiny; its correctness and novelty are not certified by these disclosures or by repository acceptance.

Relationship to companion manuscripts. The other parts of this series are Part I [2], and Part II [3]. They are cited as unpublished companion manuscripts; no public identifier or acceptance is claimed. Each part has its own hypotheses and scope. The series is not asserted to be a chain of special-case theorems.

Availability of reproducibility material. A separate versioned package has been prepared with the Lean source, dependency lockfiles, numerical code, and archived results. No public repository URL or archive identifier has been assigned to that package at the preparation date of this manuscript. The mathematical source submitted to Hexagon does not itself contain the Lean project.

References

[1] Charles S. Peskin. The immersed boundary method. *Acta Numerica*, 11:479–517, 2002. doi: 10.1017/S0962492902000077.

[2] Sida He. Stability and convergence of a regularized immersed boundary method under dynamic cartesian refinement. Part I: Fixed geometry, 2026. Unpublished companion manuscript, preparation version 0.3.3, 27 October 2026.

[3] Sida He. Stability and convergence of a regularized immersed boundary method under dynamic cartesian refinement. Part II: General prescribed motion, 2026. Unpublished companion manuscript, preparation version 0.1.1, 27 October 2026.

[4] Roland Glowinski, Tsorng-Whay Pan, Todd I. Hesla, Daniel D. Joseph, and Jacques Périaux. A fictitious domain approach to the direct numerical simulation of incompressible viscous flow past moving rigid bodies: application to particulate flow. *Journal of Computational Physics*, 169(2):363–426, 2001. doi: 10.1006/jcph.2000.6542.

[5] Bakytzhan Kallemov, Amneet Pal Singh Bhalla, Boyce E. Griffith, and Aleksandar Donev. An immersed boundary method for rigid bodies. *Communications in Applied Mathematics and Computational Science*, 11(1):79–141, 2016. doi: 10.2140/camcos.2016.11.79. URL https://arxiv.org/abs/1505.07865.

[6] Jorge San Martín, Jean-François Scheid, Takéo Takahashi, and Marius Tucsnak. Convergence of the Lagrange–Galerkin method for the equations modelling the motion of a fluid-rigid system. *SIAM Journal on Numerical Analysis*, 43(4):1536–1571, 2005. doi: 10.1137/S0036142903438161.

[7] Guillaume Legendre and Takéo Takahashi. Convergence of a Lagrange–Galerkin method for a fluid-rigid body system in ALE formulation. *ESAIM: Mathematical Modelling and Numerical Analysis*, 42(4):609–644, 2008. doi: 10.1051/m2an:2008020.

[8] Jorge San Martín, Jean-François Scheid, and Loredana Smaranda. A modified Lagrange–Galerkin method for a fluid-rigid system with discontinuous density. *Numerische Mathematik*, 122(2):341–382, 2012. doi: 10.1007/s00211-012-0460-1.

[9] C. Bost, G.-H. Cottet, and E. Maitre. Convergence analysis of a penalization method for the three-dimensional motion of a rigid body in an incompressible viscous fluid. *SIAM Journal on Numerical Analysis*, 48(4):1313–1337, 2010. doi: 10.1137/090767856.

[10] Henry von Wahl and Thomas Richter. Error analysis for a parabolic PDE model problem on a coupled moving domain in a fully Eulerian framework. *SIAM Journal on Numerical Analysis*, 61(1):286–314, 2023. doi: 10.1137/21M1458417.

[11] Daniele Boffi, Nicola Cavallini, and Lucia Gastaldi. The finite element immersed boundary method with distributed Lagrange multiplier. *SIAM Journal on Numerical Analysis*, 53(6): 2584–2604, 2015. doi: 10.1137/140978399. URL https://arxiv.org/abs/1407.5184.

[12] Daniele Boffi and Lucia Gastaldi. A fictitious domain approach with Lagrange multiplier for fluid-structure interactions. *Numerische Mathematik*, 135:711–732, 2017. doi: 10.1007/s00211-016-0814-1.

[13] Andreas Brenner, Eberhard Bänsch, and Markus Bause. A priori error analysis for finite element approximations of the Stokes problem on dynamic meshes. *IMA Journal of Numerical Analysis*, 34(1):123–146, 2014. doi: 10.1093/imanum/drt001. URL https://d-nb.info/1113290293/34.

[14] Tomas Lundquist, Jan Nordström, and Arnaud Malan. Stable dynamical adaptive mesh refinement. *Journal of Scientific Computing*, 86:43, 2021. doi: 10.1007/s10915-021-01414-1.

[15] Evan S. Gawlik and Adrian J. Lew. Unified analysis of finite element methods for problems with moving boundaries. *SIAM Journal on Numerical Analysis*, 53(6):2822–2846, 2015. doi: 10.1137/140990437. URL https://webpages.scu.edu/ftp/egawlik/pdf/GaLe2015c.pdf.

[16] Stefano Berrone, Andrea Bonito, Rob Stevenson, and Marco Verani. An optimal adaptive fictitious domain method. *Mathematics of Computation*, 88:2101–2134, 2019. doi: 10.1090/mcom/3414.

[17] Luca Heltai and Wenyu Lei. Adaptive finite element approximations for elliptic problems using regularized forcing data. *SIAM Journal on Numerical Analysis*, 61(2):431–456, 2023. doi: 10.1137/21M1455991. URL https://arxiv.org/abs/2110.15029.

[18] Yoichiro Mori. Convergence proof of the velocity field for a Stokes flow immersed boundary method. *Communications on Pure and Applied Mathematics*, 61(9):1213–1263, 2008. doi: 10.1002/cpa.20233.

[19] Yang Liu and Yoichiro Mori. Properties of discrete delta functions and local convergence of the immersed boundary method. *SIAM Journal on Numerical Analysis*, 50(6):2986–3015, 2012. doi: 10.1137/110836699.

[20] Yang Liu and Yoichiro Mori. L^p convergence of the immersed boundary method for stationary Stokes problems. *SIAM Journal on Numerical Analysis*, 52(1):496–514, 2014. doi: 10.1137/130911329.

[21] Zhilin Li, Kejia Pan, and Juan Ruiz-Álvarez. Convergence study of IB methods for Stokes equations with prescribed velocity boundary conditions. *IMA Journal of Numerical Analysis*, 45(6):3766–3799, 2025. doi: 10.1093/imanum/drae101.

[22] Luca Heltai and Wenyu Lei. A priori error estimates of regularized elliptic problems. *Numerische Mathematik*, 146(3):571–596, 2020. doi: 10.1007/s00211-020-01152-w. URL https://arxiv.org/abs/1911.02293.

[23] Alexandre Ern and Jean-Luc Guermond. *Finite Elements I: Approximation and Interpolation*, volume 72 of *Texts in Applied Mathematics*. Springer, Cham, 2021. doi: 10.1007/978-3-030-56341-7.

[24] Erik Burman, Peter Hansbo, and Mats G. Larson. Cut Bogner–Fox–Schmit elements for plates. *Advanced Modeling and Simulation in Engineering Sciences*, 7:27, 2020. doi: 10.1186/s40323-020-00164-3.

[25] Alexandre M. Roma, Charles S. Peskin, and Marsha J. Berger. An adaptive version of the immersed boundary method. *Journal of Computational Physics*, 153(2):509–534, 1999. doi: 10.1006/jcph.1999.6293.

[26] Yadong Zeng, Amneet Pal Singh Bhalla, and Lian Shen. A subcycling/non-subcycling time advancement scheme-based DLM immersed boundary method framework for solving single and multiphase fluid–structure interaction problems on dynamically adaptive grids. *Computers & Fluids*, 238:105358, 2022. doi: 10.1016/j.compfluid.2022.105358.

[27] Amal Alphonse, Charles M. Elliott, and Björn Stinner. An abstract framework for parabolic PDEs on evolving spaces. *Portugaliae Mathematica*, 72(1):1–46, 2015. doi: 10.4171/PM/1955. URL https://arxiv.org/abs/1403.4500.

[28] Ana Djurdjevac, Carsten Gräser, and Philip J. Herbert. An evolving space framework for Oseen equations on a moving domain. *ESAIM: Mathematical Modelling and Numerical Analysis*, 57(5):3113–3138, 2023. doi: 10.1051/m2an/2023074. URL https://arxiv.org/abs/2106.08312.

[29] Christoph Lehrenfeld and Maxim Olshanskii. An Eulerian finite element method for PDEs in time-dependent domains. *ESAIM: Mathematical Modelling and Numerical Analysis*, 53 (2):585–614, 2019. doi: 10.1051/m2an/2018068.

[30] Erik Burman, Stefan Frei, and Andre Massing. Eulerian time-stepping schemes for the non-stationary Stokes equations on time-dependent domains. *Numerische Mathematik*, 150:423–478, 2022. doi: 10.1007/s00211-021-01264-x. URL https://arxiv.org/abs/1910.03054.

[31] Henry von Wahl, Thomas Richter, and Christoph Lehrenfeld. An unfitted Eulerian finite element method for the time-dependent Stokes problem on moving domains. *IMA Journal of Numerical Analysis*, 42(3):2505–2544, 2022. doi: 10.1093/imanum/drab044. URL https://arxiv.org/abs/2002.02352.

[32] Qiqi Rao, Jilu Wang, and Yupei Xie. Optimal convergence of arbitrary Lagrangian–Eulerian finite element methods for the Stokes equations in an evolving domain. *IMA Journal of Numerical Analysis*, 45(6):3616–3642, 2025. doi: 10.1093/imanum/drae097.

[33] Sida He, Zixuan Yang, Fotis Sotiropoulos, and Lian Shen. Numerical simulation of interaction between multiphase flows and thin flexible structures. *Journal of Computational Physics*, 448:110691, 2022. doi: 10.1016/j.jcp.2021.110691.

[34] Kaiyuan Zheng, Sida He, Xizeng Zhao, Lian Shen, and Xiaojue Zhu. Free-surface-induced ground effect for flapping swimmers. *Journal of Fluid Mechanics*, 997:A36, 2024. doi: 10.1017/jfm.2024.830.

[35] Dandan Yang, Sida He, Lian Shen, and Xianwu Luo. Large eddy simulation coupled with immersed boundary method for turbulent flows over a backward facing step. *Proceedings of the Institution of Mechanical Engineers, Part C: Journal of Mechanical Engineering Science*, 235(15):2705–2714, 2021. doi: 10.1177/0954406220954892.

[36] Jichang Chen, Zhiwei Lu, Bin Wu, Sida He, Tianhang Xiao, Mingbo Tong, and Kan Kan. Flow transition and vortex evolution of a symmetric airfoil at low Reynolds number and high angle of attack. *Physics of Fluids*, 37(2):023603, 2025. doi: 10.1063/5.0246708.

[37] Sida He, Han Liu, and Lian Shen. Simulation-based study of turbulent aquatic canopy flows with flexible stems. *Journal of Fluid Mechanics*, 947:A33, 2022. doi: 10.1017/jfm.2022.655.

[38] L. E. Payne and H. F. Weinberger. An optimal Poincaré inequality for convex domains. *Archive for Rational Mechanics and Analysis*, 5:286–292, 1960. doi: 10.1007/BF00252910.

[39] Kambiz Salari and Patrick Knupp. Code verification by the method of manufactured solutions. Technical Report SAND2000-1444, Sandia National Laboratories, 2000.

[40] Leonardo de Moura and Sebastian Ullrich. The Lean 4 theorem prover and programming language. In *Automated Deduction—CADE 28*, volume 12699 of *Lecture Notes in Computer Science*, pages 625–635, Cham, 2021. Springer. doi: 10.1007/978-3-030-79876-5_37.

[41] The mathlib Community. The Lean mathematical library. In *Proceedings of the 9th ACM SIGPLAN International Conference on Certified Programs and Proofs*, CPP '20. ACM, 2020. doi: 10.1145/3372885.3373824.